THE SAGES LEGACY UNIFYING GLOBULARS AND GALAXIES SURVEY (SLUGGS): SAMPLE DEFINITION, METHODS, AND INITIAL RESULTS

Jean P. Brodie[1], Aaron J. Romanowsky[1,2], Jay Strader[3], Duncan A. Forbes[4], Caroline Foster[5], Zachary G. Jennings[1],
Nicola Pastorello[4], Vincenzo Pota[1,4], Christopher Usher[4], Christina Blom[4], Justin Kader[1], Joel C. Roediger[1],
Lee R. Spitler[5,6], Alexa Villaume[1], Jacob A. Arnold[1], Sreeja S. Kartha[4], and Kristin A. Woodley[1]

[1] University of California Observatories, 1156 High Street, Santa Cruz, CA 95064, USA; jbrodie@ucsc.edu
[2] Department of Physics and Astronomy, San José State University, One Washington Square, San Jose, CA 95192, USA
[3] Department of Physics and Astronomy, Michigan State University, East Lansing, MI 48824, USA
[4] Centre for Astrophysics and Supercomputing, Swinburne University, Hawthorn, VIC 3122, Australia
[5] Australian Astronomical Observatory, P.O. Box 915, North Ryde, NSW 1670, Australia
[6] Department of Physics and Astronomy, Macquarie University, North Ryde, NSW 2109, Australia

ABSTRACT

We introduce and provide the scientific motivation for a wide-field photometric and spectroscopic chemodynamical survey of nearby early-type galaxies (ETGs) and their globular cluster (GC) systems. The SAGES Legacy Unifying Globulars and GalaxieS (SLUGGS) survey is being carried out primarily with Subaru/Suprime-Cam and Keck/ DEIMOS. The former provides deep gri imaging over a 900 arcmin^2 field-of-view to characterize GC and host galaxy colors and spatial distributions, and to identify spectroscopic targets. The NIR Ca II triplet provides GC line-of-sight velocities and metallicities out to typically $\sim 8~R_e$, and to $\sim 15~R_e$ in some cases. New techniques to extract integrated stellar kinematics and metallicities to large radii (~ 2–$3~R_e$) are used in concert with GC data to create two-dimensional (2D) velocity and metallicity maps for comparison with simulations of galaxy formation. The advantages of SLUGGS compared with other, complementary, 2D-chemodynamical surveys are its superior velocity resolution, radial extent, and multiple halo tracers. We describe the sample of 25 nearby ETGs, the selection criteria for galaxies and GCs, the observing strategies, the data reduction techniques, and modeling methods. The survey observations are nearly complete and more than 30 papers have so far been published using SLUGGS data. Here we summarize some initial results, including signatures of two-phase galaxy assembly, evidence for GC metallicity bimodality, and a novel framework for the formation of extended star clusters and ultracompact dwarfs. An integrated overview of current chemodynamical constraints on GC systems points to separate, in situ formation modes at high redshifts for metal-poor and metal-rich GCs.

Key words: galaxies: abundances – galaxies: elliptical and lenticular, cD – galaxies: halos – galaxies: kinematics and dynamics – galaxies: star clusters: general – globular clusters: general

Online-only material: color figures

1. INTRODUCTION AND SCIENTIFIC MOTIVATION

Recent advances in both observations and theory of early-type galaxies (ETGs; ellipticals and lenticulars) have begun to revolutionize our understanding of these systems as more than simply "red and dead" (where star formation has long since ceased). High-redshift (z) studies have revealed an unexpectedly strong systematic size evolution, where galaxies in the early universe were much denser and more compact than their present-day counterparts (e.g., Daddi et al. 2005; van Dokkum et al. 2009). These observations are now widely understood on theoretical grounds to reflect a "two-phase" or "inside-out" formation history, where an early, rapid phase of assembly and star formation establishes the cores of galaxies (on ~ 1 kpc scales), followed by a protracted expansion of the galaxy through minor mergers (as opposed to a simple major-merger scenario; Khochfar & Silk 2006; Naab et al. 2009; Hopkins et al. 2010; Oser et al. 2010, 2012; Johansson et al. 2012; Lackner et al. 2012; Hilz et al. 2012, 2013; Gabor & Davé 2012; Oogi & Habe 2013; Bédorf & Portegies Zwart 2013; Dekel & Burkert 2014; Porter et al. 2014; but see Nipoti et al. 2012).

This picture may be tested and refined further through observations of low-z galaxies, whose outer regions are natural proving grounds for the later accretion phase of galaxy assembly, owing to the long dynamical timescales (Figure 1) and more recent putative activity in these regions.

Various studies have pursued this idea by searching for transitions and substructures in the stellar halos of nearby ETGs (e.g., Forbes & Thomson 1992; Mihos et al. 2005, 2013; Harris et al. 2007; Tal et al. 2009; Coccato et al. 2010; Mouhcine et al. 2011; La Barbera et al. 2012; Huang et al. 2013; Greene et al. 2013; D'Souza et al. 2014).

In this context, what has been missing is a dedicated, systematic survey of the wide-field chemodynamics of nearby ETGs, akin to the SAURON and ATLAS^{3D} surveys (de Zeeuw et al. 2002; Cappellari et al. 2011) but on much larger spatial scales. These surveys, like the vast majority of ETG studies, have focused on the central regions, well inside an effective radius R_e that encloses half of a galaxy's projected stellar mass or luminosity. By definition, this misses over half of the stars, including virtually all those in the crucial halo regions.

More acutely, dynamical studies of halos are required to constrain two of the most fundamental parameters that characterize a galaxy: the stellar angular momentum and the total mass (including dark matter), which are typically only $\sim 10\%$ and $\sim 5\%$ contained inside $1~R_e$, respectively (Figure 1). The halo mass is a key controlling parameter in galaxy formation models. However, connections between ordinary ETGs and their halo masses are usually made only on a statistical (rather than individual) basis, and often through indirect means (e.g., Yang et al. 2005). The angular momentum traces torques in galaxy formation and is an important benchmark for theoretical models
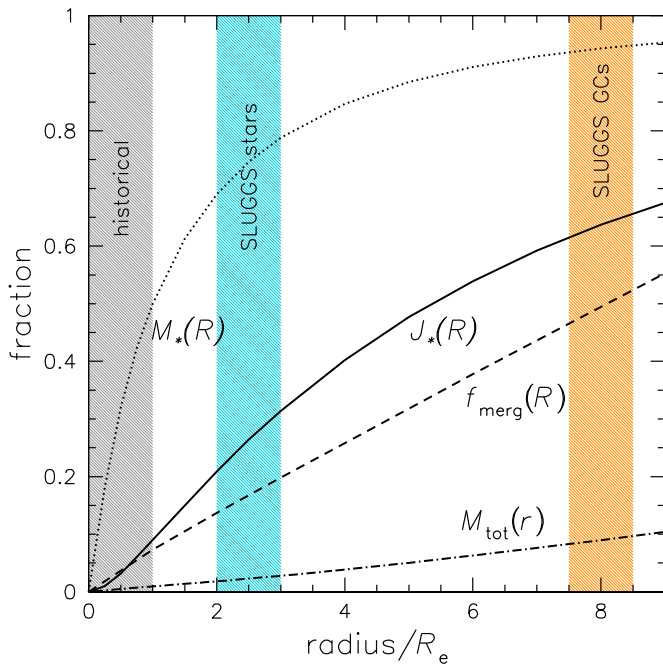
Figure 1. Cumulative fraction of physical quantities vs. radius in an ordinary elliptical galaxy. The galaxy is approximated as a very simple $R^{1/4}$ projected density profile with a rotation velocity that is constant with radius. The projected stellar mass and angular momentum profiles are thus shown as $M_*(R)$ and $J_*(R)$. The total mass profile including dark matter, $M_{tot}(r)$, and the probability of detectable substructure at a given radius, $f_{merg}(R)$, are derived from cosmologically based models (Sections 4.3 and 5.1). The shaded area at left reaches out to one effective radius, the typical extent of detailed galaxy kinematics studies to date, which therefore miss ~50% of M_*, ~90% of J_*, ~99% of M_{tot}, and ~93% of the potential merging signatures. The other shaded areas show the radii reached by SLUGGS—capturing much larger fractions of these important parameters.

(A color version of this figure is available in the online journal.)

(e.g., Mestel 1963; Fall & Efstathiou 1980; Navarro & Steinmetz 1997; Governato et al. 2004; Obreschkow & Glazebrook 2014), but estimates of its total value in ETGs have so far been based on a hodge podge of inhomogeneous data from the literature (Romanowsky & Fall 2012).

Pushing spectroscopy out into the halos of ETGs is very challenging because of the low surface brightness levels of the stellar light, with maximum galactocentric radii of ~4 R_e currently attainable. Beyond these radii, it is necessary to use a bright discrete tracer population. Planetary nebulae (PNe) are one useful option for kinematical constraints, (e.g., Douglas et al. 2002; Peng et al. 2004b; Coccato et al. 2009; McNeil et al. 2010; Ventimiglia et al. 2011) but using them to probe stellar populations is observationally expensive (e.g., Méndez et al. 2005).

Globular clusters (GCs) have a distinguished history as indicators of the assembly histories of galaxy halos, for the Milky Way and beyond (Searle & Zinn 1978; Brodie & Huchra 1991; Abadi et al. 2006; Brodie & Strader 2006; Forbes & Bridges 2010). They provided evidence that ETG evolution was driven by minor rather than major mergers, long before this became the mainstream model (Forte et al. 1982; Côté et al. 1998; Kissler-Patig et al. 1998). They have also long been used to infer the presence and properties of metal-poor stellar halos, which are a subject of intense interest in galaxy formation (e.g., Bullock & Johnston 2005; Cooper et al. 2010) but which have been very challenging to study directly even in the nearest

galaxies (e.g., Kalirai et al. 2006; Harris et al. 2007; Mihos et al. 2013; Ibata et al. 2014).

Many insightful imaging studies of GCs have been carried out using the *Hubble Space Telescope* (*HST*, which generally covers only the central regions of galaxies; e.g., Larsen et al. 2001; Kundu & Whitmore 2001; Peng et al. 2006; Strader et al. 2006; Mieske et al. 2010), and from the ground (which affords a much wider field of view; e.g., Forte et al. 2007; Hargis & Rhode 2012). However, there has so far not been a homogeneous *spectroscopic* survey of GC systems for a large sample of ETGs covering the full range of environments.

1.1. SLUGGS

Into this void, we have launched the SAGES Legacy Unifying Globulars and GalaxieS (SLUGGS)[7] survey. The survey uses a combination of imaging from Subaru/Suprime-Cam and spectroscopy from Keck/DEIMOS to obtain the *spatial*, *kinematical*, and *chemical* properties of both *diffuse stellar light* and *GCs* in two dimensions and over wide areas around 25 nearby ETGs spanning a broad range of galaxy properties and environments.

Some aspects of the survey, such as the GC imaging and spectroscopy, build on established observational techniques and apply them with great success using state-of-the-art instrumentation. Other aspects are novel and potentially transformative for the study of nearby galaxies. These involve Stellar Kinematics from Multiple Slits (SKiMS), a technique that we have pioneered to map out the kinematics and metallicities of diffuse starlight in two dimensions (2D) to large radii (e.g., Norris et al. 2008; Proctor et al. 2008, 2009).

All of the spectroscopic aspects of the survey exploit the strong Ca II triplet absorption line feature in the near-infrared (~8500 Å), where DEIMOS has both a high efficiency and a high spectral resolution for separating the galaxy and GC lines from the forest of near-infrared sky lines.

The main advantages of the SLUGGS survey are the superior velocity precision (median 12 km s^{-1}) on a very stable, high-throughput instrument, and the large radial coverage (typically ~2–3 R_e for stars, extending to ~8 R_e when GCs are included).

1.2. Survey Comparisons

In Figure 2 and Table 1 we have summarized other current and planned 2D chemodynamical surveys of ETGs. These surveys use either an Integral Field Unit (IFU) or a fiber-bundle. We briefly discuss these in turn.

Building on the success of the original SAURON survey, the ATLAS^{3D} survey (Cappellari et al. 2011) of 260 nearby ETGs has had a high scientific impact. However, it has a moderate velocity resolution of 105 km s^{-1} (limiting its ability to map both low-mass galaxies and kinematically cold features in all galaxies) and, perhaps most importantly, a small field-of-view. To compensate for this, galaxies were often targeted with two pointings, giving a median extent for the survey observations of 0.9 R_e. For more luminous and nearby galaxies, comparable to those in SLUGGS, the typical extent is only 0.6 R_e (see Figure 1 in Arnold et al. 2014).

A recently initiated survey comprising all galaxy types using the SAMI instrument (Bryant et al. 2014) will increase the number of ETGs mapped with higher velocity resolution and wider wavelength coverage, but will not reach much beyond

---

Table 1
Two-dimensional Chemo-dynamical Surveys

Survey	SLUGGS	ATLAS[3D]	VIRUS–P	MASSIVE	CALIFA	SAMI	MaNGA
Completion year	2015	2008	2014	>2014	2015	2016	2020
No. of ETGs	25	260	50	116	80	1700	3500, 1500
Distance (Mpc)	<30	<42	40–95	17–108	20–120	∼170	∼130
Radial extent (R_e)	2.5, 8	0.9	2.5	2.1	2	1.7	1.5, 2.5
Vel. res. σ (km s^{-1})	24	98	150	150	69	73	64
Wavelengths (Å)	6500–9100	4800–5380	3550–5850	3550–5850	3700–5000	3700–5700	3600–10,000

Notes. Rows give survey or instrument name, expected year of completion of data acquisition, number of early-type galaxies (ETGs) studied (note that there are two different radial extents in SLUGGS for stars and GCs, and in MaNGA for the primary and secondary samples), typical distance of sample, typical radial extent probed, instrumental velocity resolution σ (note that SAMI also has higher resolution coverage at redder wavelengths that is used for emission-line mapping rather than integrated stellar spectroscopy), and total wavelength range.
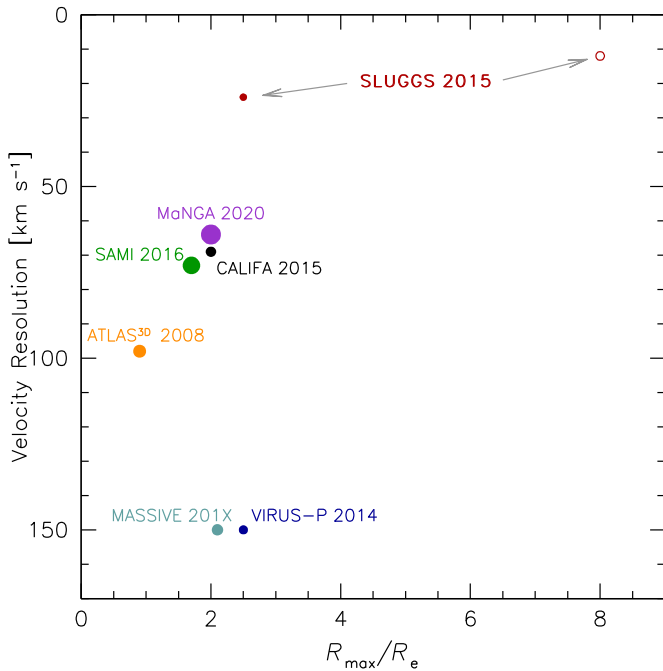

Figure 2. SLUGGS survey figure of merit. Instrumental velocity resolution (σ) is plotted (with superior resolution at the top) vs. maximum galactocentric radial extent for a typical survey galaxy, in units of effective radii. The symbols show the different 2D chemodynamical surveys with their data completion dates indicated in the legend. Symbols are scaled by the log of the number of early-type galaxies surveyed. The open circle represents the globular cluster aspect of the SLUGGS survey. For the MaNGA survey we have combined the primary and secondary samples. SLUGGS is complementary to previous, or currently underway, 2D spectroscopic surveys; it covers a more limited number of galaxies but offers better radial coverage and higher velocity resolution.

(A color version of this figure is available in the online journal.)

$1 R_e$. As noted earlier, most of the mass and angular momentum in ETGs is located beyond $1 R_e$, where we also expect key signatures of galaxy formation.

A number of surveys are probing beyond $1 R_e$. CALIFA (Sánchez et al. 2012) is well underway and, upon completion (expected in 2015), around 80 ETGs will have been observed out to about $2 R_e$ with a velocity resolution of 69 km s^{-1} (blue arm).

Perhaps most comparable to SLUGGS is the study of 50 nearby ETGs that uses the Mitchell Spectrograph IFU (formerly VIRUS-P; Greene et al. 2013; Raskutti et al. 2014). This study operates in the optical and so is capable of obtaining both age and metallicity information, as well as kinematics, out to ∼2.5 R_e. The drawbacks are the relatively poor velocity resolution (150 km s^{-1}) and the lower signal-to-noise ratio

(S/N) at large radii, which inhibits the 2D coverage. A follow-up survey, MASSIVE, is focusing on galaxies at the extreme high end of the stellar mass range (Ma et al. 2014).

Due to start in 2014 and collect data for six years, the MaNGA survey (PI Kevin Bundy, http://www.sdss3.org/future/manga.php) will map an impressive 10,000 galaxies, roughly half of which will be ETGs. It will cover UV to near-IR wavelengths (3600–10,000 Å) with a velocity resolution of 64 km s^{-1}. Although it will reach only about 1.5 R_e for the primary sample, a secondary sample of ∼1500 will be observed to 2.5 R_e.

Partially overlapping with SLUGGS both in theme and in galaxy sample is the Next Generation Virgo Cluster Survey (NGVS), a multi-band photometric study of the Virgo cluster with an emphasis on GCs (Ferrarese et al. 2012). However, NGVS does not incorporate a full, systematic spectroscopic component, which is the main focus of our survey, along with an exploration of galaxies in a wide range of environments.

1.3. This Paper

The SLUGGS survey has been designed to address the following science themes: What are the basic, global chemodynamical properties of ETGs? (including their masses, angular momenta, orbital structures, and metallicities over a wide range in radius). What is the distribution of dark matter in ETGs? How are the outer regions of ETGs assembled? How does ETG assembly depend on mass, environment, and other variables? Do the observations agree with theoretical models of galaxy formation?

SLUGGS began as a pilot project in 2006 November, using DEIMOS to measure velocities of GCs around the giant elliptical NGC 1407 (Romanowsky et al. 2009). Since then it has evolved into a full survey, leading to over 30 papers to date (many of them discussed below), with the first large installments of data coming in Usher et al. (2012) on GC metallicities, Pota et al. (2013) on GC kinematics, Arnold et al. (2014) on stellar kinematics, and Pastorello et al. (2014) on stellar metallicities.

As a preview of the nature and quality of the SLUGGS results, Figure 3 shows the observed 2D stellar velocity field of a galaxy, zooming out to show different types of data on three spatial scales. The inner regions of the data come from the well-known SAURON integral field spectrograph, the intermediate regions are from SKiMS, and the outer regions come from GCs. The SKiMS data show initially the same pattern as SAURON out to $1 R_e$, with a disklike rotation pattern that is well-aligned with the isophotes. However, by $2 R_e$, there are indications of a kinematic twist that becomes even more prominent in the GC data at ∼5 R_e where there are additional asymmetries that suggest unrelaxed post-merger material. Thus at large radii, we see the emergence
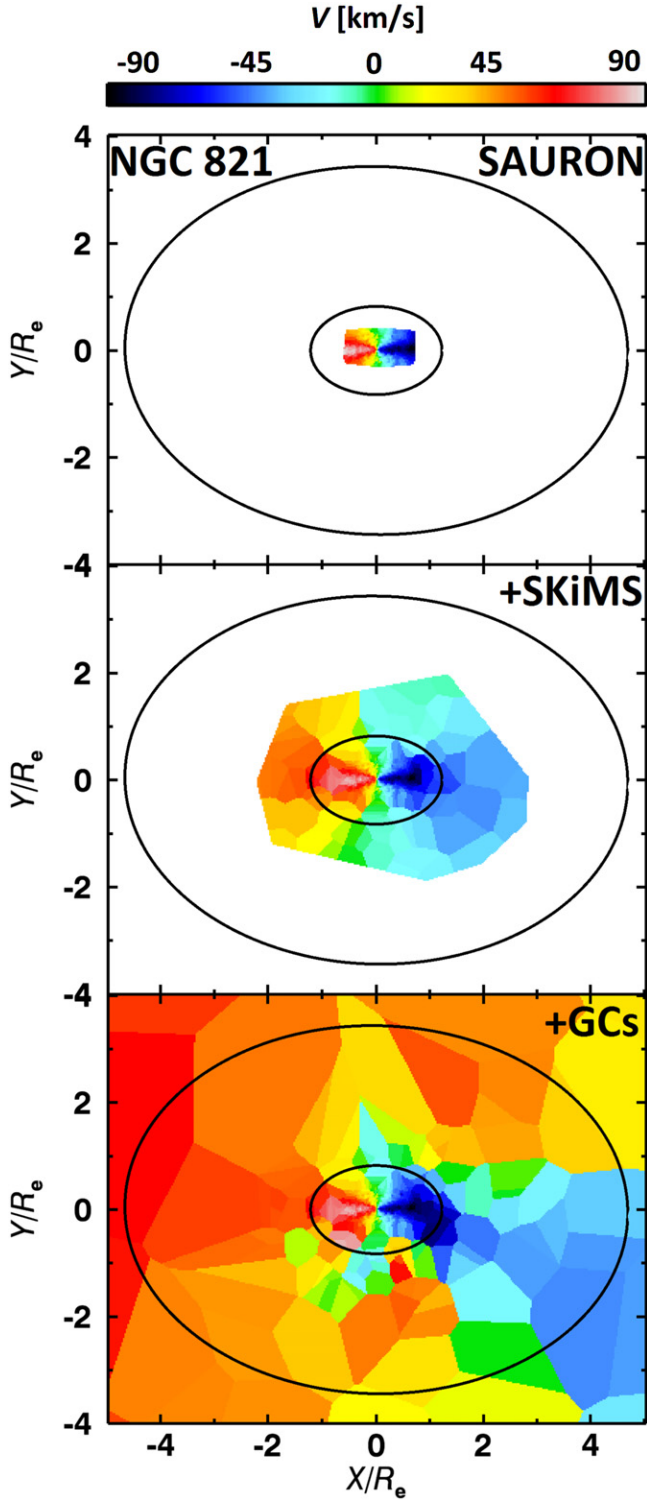
Figure 3. Stellar mean line-of-sight velocity field of the elliptical galaxy NGC 821, where the color scale indicates the velocity amplitude (see scale bar at top). Ellipses mark schematic isophotes at 1 R_e and 4 R_e; the axes are aligned with the 1 R_e ellipse (major-axis sky P.A. = 30°5). The top panel shows an ATLAS^{3D}/SAURON pointing of the central region (Cappellari et al. 2011), the middle panel incorporates the intermediate-radius regions reconstructed from SLUGGS/DEIMOS data using the SKiMS (stellar kinematics with multiple slits) technique along with major- and minor-axis long-slit data from the literature, and the bottom panel folds in GC velocities to large radii. Note that the SLUGGS methods have sparser spatial sampling than a true integral-field unit, requiring some smoothing in creating these maps (described in A. J. Romanowsky et al., in preparation). The central regions do not reveal the kinematic twisting and complexity that are apparent in the wide-field map.

(A color version of this figure is available in the online journal.)

of new information about the galaxy structure and formation that is not apparent from the central regions alone.

This paper provides a general overview of SLUGGS, including the galaxy sample definition (Section 2) and summaries of our observing and data reduction techniques (Section 3), and modeling methods (Section 4). Some initial results are presented in Section 5 and conclusions are provided in Section 6. An Appendix provides further details about the galaxy sample. More information and news can be found on the survey Web site.[8]

2. GALAXY SAMPLE SELECTION AND PROPERTIES

Even with the best current observing resources, a proper volume- and magnitude-limited spectroscopic survey (like ATLAS^{3D}) is unfeasible for a study of GCs, so following the original SAURON survey (de Zeeuw et al. 2002), we explore a "representative" sample of 25 ETGs (Figure 4 and Table 2). The strategy here is to consider the relevant basic parameters of these galaxies, and to identify the controlling factors for their formation histories and present-day properties. Despite the limited pool of galaxies in the nearby universe (within ∼25 Mpc), our sample has been constructed to provide excellent coverage of parameter space and to embrace the regime of "ordinary" ETGs of the characteristic L^* luminosity. These galaxies in particular have so far been the subject of very little GC spectroscopy.

Our selection parameters are described below. They are all based on broad properties of the visible and near-infrared galactic stellar light, and are chosen for their probable importance in galactic evolution, as well as for their general availability in the literature for nearby galaxies. Where possible, we adopt the same parameters used in the ATLAS^{3D} survey to provide a clear context for how the SLUGGS sample fits in with the general population of galaxies in the nearby universe. For the sake of homogeneity, the parameter values are *not* always the most accurate that are available, as will be discussed further.

The first galaxy parameter is the K-band absolute magnitude, M_K, which for ETGs is a very good proxy for stellar mass at the ∼10% level (e.g., Fall & Romanowsky 2013). These values are based on the Two Micron All Sky Survey (2MASS; Jarrett et al. 2000), with further details provided in the Appendix. Here it should be noted that the 2MASS photometry is known to systematically underestimate galaxy luminosities by ∼10%–40%, particularly for the most nearby, extended galaxies, due to over-subtracting the sky background (e.g., Devereux et al. 2009; Scott et al. 2013). Although this effect can be corrected for (e.g., Romanowsky et al. 2012), it is best done by using homogeneous model fits to the galaxy light profiles, which are not yet available for our sample. Nonetheless, based on the scatter around the correction derived by Scott et al. (2013), $K_{new} = 1.07 \times K_{old} + 1.53$, we expect the relative luminosity values to be accurate to within ∼0.2 mag.

For absolute magnitudes, galaxy distances are needed, which we base on analyses of surface brightness fluctuations (SBF; Tonry et al. 2001; Blakeslee et al. 2009). The distances in our sample range from 9 Mpc (NGC 3115) to 27 Mpc (NGC 720, NGC 1400 and NGC 1407), with the median being 17 Mpc. The luminosity range is from $M_K = -22.3$ ($L_K = 2 \times 10^{10} L_{K,\odot}$; NGC 4474) to $M_K = -25.5$ ($L_K = 3 \times 10^{11} L_{K,\odot}$; NGC 1407), with a median of $M_K = -24.0$ ($L_K = 8 \times 10^{10} L_{K,\odot}$; NGC 1023).

Further details of the magnitudes and distances are discussed in the Appendix, along with other parameters presented
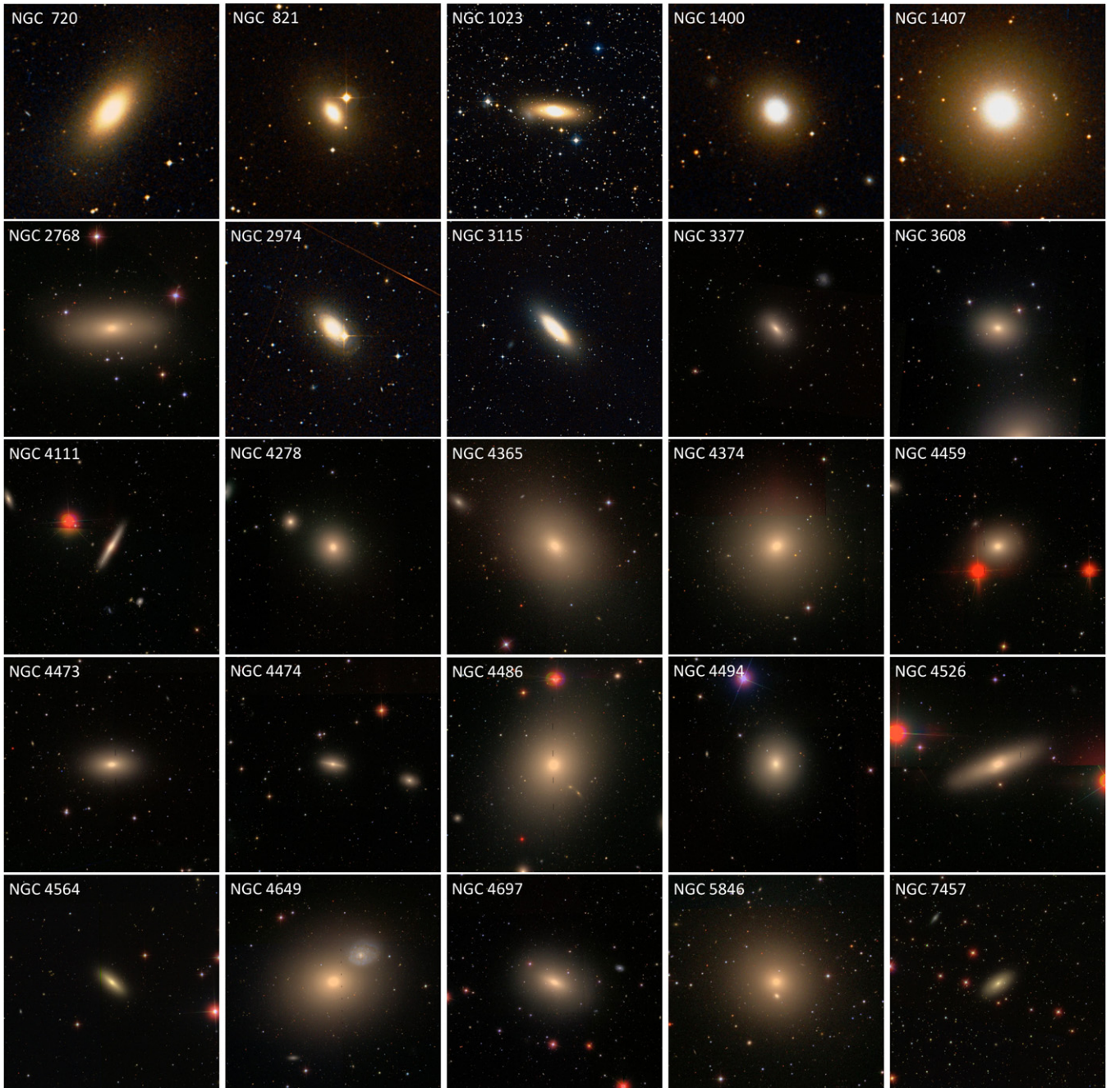

Figure 4. Color thumbnails of the SLUGGS survey sample of galaxies, from the SDSS where available and otherwise from the DSS (provided via http://www.wikisky.org).The field-of-view in each case is 70×70 kpc. North is up and east to the left. The galaxy identifications are as labeled in the panels.

(A color version of this figure is available in the online journal.)

in Table 2, including the central velocity dispersion, the effective radius, the morphology, various isophote parameters, the recession velocity, and environmental parameters. For some of these parameters (dispersion, etc.), there is an arbitrary choice of spatial scale. We generally select whatever scale is homogeneously available from the literature (including ATLAS^{3D} in particular) while being as close to $1\,R_e$ as possible.

As a concise summary of the galaxy sample selection, Figure 5 shows the parameter space of luminosity and rotation, marking both the SLUGGS galaxies and the full ATLAS^{3D} sample for reference.

Here the classic distinction between slow and fast rotators is evident, with almost all galaxies above and below $\sim 2\,L^*$

luminosity having V/σ less than and greater than 0.15, respectively. Our sample includes a large fraction of the luminous slow rotators—which have been the classic target of GC spectroscopy for decades—while now also extending to L^* luminosities and below. Among the less luminous galaxies, our sample has a bias toward the more rotationally dominated systems. This is effectively a selection effect for more edge-on inclinations that we adopted in order to reduce the ambiguity with galaxy deprojection.

The remainder of the galaxy parameters are discussed and diagramed in the Appendix, where it can be seen that SLUGGS samples the parameter space very well, with only minor quirks such as the inclination bias and an over-representation of

Table 2
SLUGGS Survey Galaxy Parameters

Galaxy NGC (1)	M_K (mag) (2)	Dist. (Mpc) (3)	σ_{kpc} (km s^{-1}) (4)	$V/\sigma_{e/2}$ (5)	R_e ($''$) (6)	Morph. (7)	T_{Hub} (8)	P.A. ($°$) (9)	ϵ (10)	a_4/a (%) (11)	γ' (12)	V_{sys} (km s^{-1}) (13)	Env. (14)	ρ_{env} (Mpc^{-3}) (15)
Main														
720	−24.88	26.9	227	0.10	35	E5	−4.9	140.0	0.49	0.00	0.07	1745	F	0.25
821	−23.99	23.4	193	0.29	40	E6	−4.8	31.2	0.35	1.43	0.51	1718	F	0.08
1023	−24.01	11.1	183	0.37	48	S0	−2.6	83.3	0.63	0.68	0.74	602	G	0.57
1400	−24.35	26.8	236	0.23	28	E1/S0	−3.7	40.0	0.13	−0.50	0.20	558	G	0.42
1407	−25.46	26.8	252	0.07	63	E0	−4.5	35.0	0.07	−0.50	0.14	1779	G	0.42
2768	−24.71	21.8	206	0.24	63	E6/S0	−4.5	91.6	0.57	−0.68	0.37	1353	G	0.31
2974	−23.62	20.9	231	0.81	38	E4/S0	−2.1	44.2	0.37	1.22	0.62	1887	F	0.26
3115	−24.00	9.4	248	0.59	35	S0	−2.9	40.0	0.66	4.00	0.52	663	F	0.08
3377	−22.76	10.9	135	0.56	36	E5–6	−4.8	46.3	0.33	0.74	0.68	690	G	0.49
3608	−23.65	22.3	179	0.05	30	E1–2	−4.8	82.0	0.20	−0.34	0.17	1226	G	0.56
4111	−23.27	14.6	161	0.66	12	S0	−1.3	150.3	0.79	4.80	. . .	792	G	1.09
4278	−23.79	15.6	228	0.21	32	E1–2	−4.8	39.5	0.09	−0.34	0.10	620	G	1.25
4365	−25.19	23.1	253	0.11	53	E3	−4.8	40.9	0.24	−0.80	0.00	1243	G	2.93
4374	−25.13	18.5	284	0.03	53	E1	−4.3	128.8	0.05	−0.27	0.25	1017	C	3.99
4459	−23.89	16.0	170	0.45	36	S0	−1.4	105.3	0.21	−0.14	0.49	1192	C	4.06
4473	−23.76	15.2	189	0.26	27	E5	−4.7	92.2	0.43	0.95	0.10	2260	C	2.17
4474	−22.27	15.5	88	0.35	17	S0	−1.9	121.2	0.42	6.26	0.57	1152	C	3.80
4486	−25.31	16.7	307	0.02	81	E0/cD	−4.3	151.3	0.16	0.13	0.23	1284	C	4.17
4494	−24.11	16.6	157	0.22	49	E1–2	−4.8	176.3	0.14	0.03	0.55	1342	G	1.04
4526	−24.61	16.4	233	0.56	45	S0	−1.9	113.7	0.76	0.10	. . .	617	C	2.45
4564	−23.08	15.9	153	0.53	20	E6	−4.8	48.5	0.53	1.88	0.81	1155	C	4.09
4649	−25.36	16.5	308	0.12	66	E2/S0	−4.6	91.3	0.16	−0.47	0.14	1110	C	3.49
4697	−24.13	12.5	180	0.36	62	E6	−4.5	67.2	0.32	1.30	0.82	1252	G	0.60
5846	−25.00	24.2	231	0.04	59	E0–1/S0	−4.7	53.3	0.08	−0.34	−0.02	1712	G	0.84
7457	−22.38	12.9	74	0.48	36	S0	−2.7	124.8	0.47	0.58	0.61	844	F	0.13
Bonus														
3607	−24.75	22.2	229	0.29	39	S0	−3.2	124.8	0.13	−0.12	0.26	942	G	0.34
4594	−24.95	9.5	225	0.57	70	Sa	+1.1	90.0	0.59	. . .	. . .	1024	F	0.32
5866	−24.00	14.9	163	0.35	36	S0	−1.2	125.0	0.58	6.19	. . .	755	G	0.24

Notes. Parameters of the 25 galaxies from the SLUGGS survey, as well as three bonus galaxies (at the bottom of the table). Details of the parameter derivations are given in Section 2 and in the Appendix. Column descriptions: (1) galaxy NGC number; (2) extinction-corrected K-band absolute magnitude; (3) distance measured in Mpc; (4) central stellar velocity dispersion within 1 kpc; (5) rotational dominance parameter within $0.5\,R_e$; (6) effective (half-light) radius; (7) morphological type; (8) Hubble stage parameter, where $T_{Hub} = -5$ for E, -3 for E/S0, -2 for S0, and 0 for S0/a; (9) position angle and (10) ellipticity, for the outer isophotes; (11) fourth-order isophote shape parameter; (12) central stellar density slope; (13) systemic velocity; (14) local environment type: field (F), group (G), or cluster (C); (15) environmental density of neighboring galaxies. Alternative names for some of the galaxies are M84 (NGC 4374), M87 (NGC 4486), M60 (NGC 4649), and M104 (NGC 4594).

ellipticals at the expense of lenticulars. We also have a mild selection effect on galaxy recession velocity, requiring $V_{sys} \gtrsim 600\,\mathrm{km\,s^{-1}}$ in order to minimize potential confusion between GCs and Galactic stars. This constraint is mainly relevant to the Virgo cluster, where the intrinsic velocity dispersion leads to some cases of very low V_{sys}, including several well-known giant ellipticals which are therefore not included in SLUGGS: NGC 4406 (M86), NGC 4472 (M49), NGC 4552 (M89), and NGC 4621 (M59).

The sample size of 25 is approximately motivated as follows. There are a minimum of three important parameter choices, bright and faint, cluster and non-cluster, fast and slow rotation, which define eight basic galaxy bins (2^3), and we have, somewhat arbitrarily, decided that we need at least three galaxies per bin. Figure 4 provides images of all the galaxies on a physically consistent spatial scale. Note that there are three additional galaxies whose properties appear at the bottom of Table 2. They are bonus galaxies that have been observed and analyzed in the same manner as those in the main survey, but they were not included in the original sample and have less extensive data sets. We list them here for completeness. Other,

smaller galaxies are also located within the survey footprints and may be studied serendipitously (e.g., NGC 4283, NGC 4468, NGC 5845).

Out of the 25 SLUGGS galaxies, 19 have photometric data available from the Sloan Digital Sky Survey (SDSS), and 21 are part of the ATLAS^{3D} survey, including a subset of 15 galaxies from the original SAURON survey (de Zeeuw et al. 2002), which was by design to benefit from synergies of combining the data sets (there are similarly 18 galaxies overlapping with PN surveys; e.g., Coccato et al. 2009; Teodorescu et al. 2011; Cortesi et al. 2013). At the time of writing, DEIMOS spectroscopy has been completed for all but three of the SLUGGS galaxies.

As a summary of one of the main achievements planned for the survey, Figure 6 shows the numbers of GCs with spectroscopy, as a function of host galaxy M_K—including a slight extrapolation for data anticipated as well as already analyzed. One sees that the L^* galaxies should each provide ~100 radial velocities, ranging to many hundreds for the largest galaxies. The symbol sizes also re-emphasize the importance of velocity precision—for allowing dynamical studies of low-mass
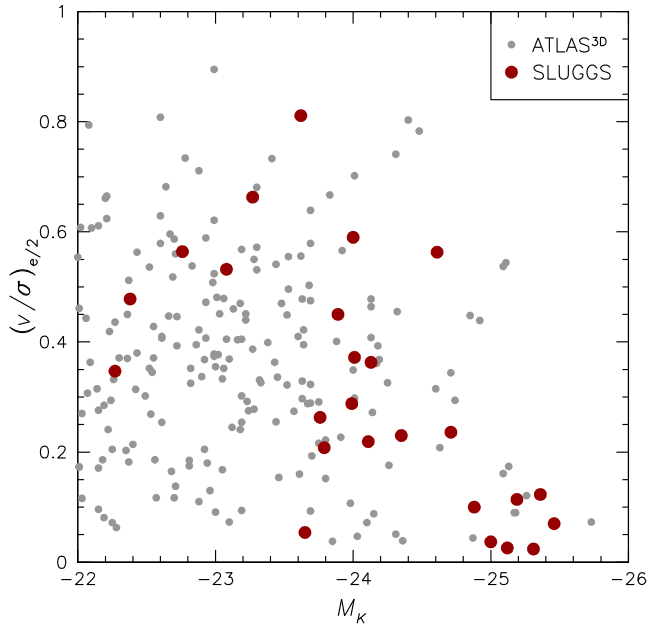
Figure 5. Rotation–luminosity space for early-type galaxies in the nearby universe. Large red points are from the SLUGGS survey; smaller gray points are from ATLAS^{3D}. $M_K \simeq -24.0$ corresponds to the characteristic luminosity L_K^*. Roughly half of the sample are ordinary L_K^* galaxies with a range of apparent rotation properties, a quarter are very luminous slow rotators, and a quarter are low-luminosity fast rotators.

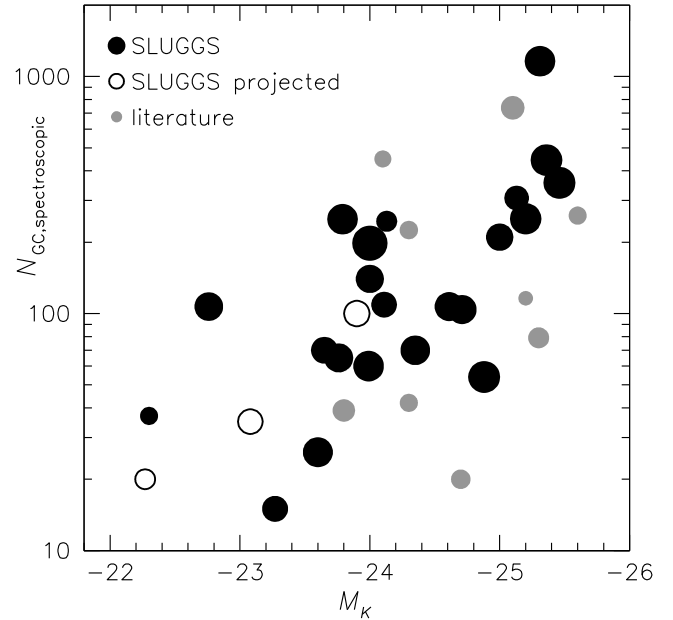(A color version of this figure is available in the online journal.)

Figure 6. Quality and scope of the SLUGGS spectroscopic sample. The plot shows the number of spectroscopically confirmed GCs vs. absolute magnitude in the K-band. The symbol sizes are scaled by the velocity precision (bigger is better: the scaling uses a logarithmic function of galaxy velocity dispersion divided by GC velocity measurement uncertainty). Filled black circles denote SLUGGS galaxies already observed and analyzed (including in some cases supplementary data from other instruments besides DEIMOS), while open circles show our projected returns for the remaining survey sample. Gray circles show all ETGs from the literature with more than 20 velocity measurements (see Pota et al. 2013 for references; note that the one well-studied L^* case is the nearby peculiar galaxy NGC 5128). The survey is obtaining high-precision velocities of ordinary GCs in large numbers, over a wide range of galaxy luminosities.

galaxies, for measuring low rotation amplitudes, and for detecting kinematically cold disks and substructures.

An important feature of SLUGGS is that most of the targeted objects (particularly for kinematics) are "ordinary" GCs, as opposed to the typical past selection of the brightest tip of the GC population. Many of these luminous objects are ultracompact dwarfs (UCDs) that have different kinematics and stellar populations than the general GC population (Section 5.3). The unrivaled efficiency of Keck/DEIMOS is a game-changer in this arena: for example, Gemini/GMOS requires 2.5 times longer aperture-adjusted exposure times for a ~1.5 mag shallower limit, over a ~2.5 times smaller field of view (Bridges et al. 2006); see also discussion in Section 3.2.2 about velocity reliability issues with other instruments. This order-of-magnitude improvement permits for the first time large spectroscopic data sets of ordinary GCs to be obtained around a large sample of galaxies.

3. DATA ACQUISITION, REDUCTION, AND ANALYSIS

The central instruments used for SLUGGS are Suprime-Cam on the 8.2 m Subaru telescope (Miyazaki et al. 2002) for imaging, and DEIMOS on the 10 m Keck II telescope (Faber et al. 2003) for spectroscopy. Here we discuss the techniques for observation and data reduction, leading to the following six basic data products from our survey: multi-color galaxy surface photometry, GC photometric catalogs, GC radial velocities, GC CaT line-strength measurements, galaxy-light kinematic moments, and galaxy-light CaT line-strength measurements.

3.1. Imaging

3.1.1. Background

High-quality imaging is an important first step for our survey, required for selecting GC candidates for follow-up spec-

troscopy. However, it is also critical for deriving robust GC surface density distributions (in 2D, including both radial profiles and ellipticities). These spatial distributions are necessary for estimating the total numbers of GCs (N_{GC}) around each galaxy and are vital ingredients in models that use GCs as kinematic tracers.

The GC systems of massive ETGs typically extend to projected radii greater than 100 kpc and require wide-field imaging covering tens of arcminutes on a side in order to obtain reasonably complete spatial coverage. Therefore, the early photographic surveys of nearby galaxies (e.g., Harris & Racine 1979) remained the state of the art for decades until modern CCD cameras reached the requisite field sizes (e.g., Rhode & Zepf 2001; Dirsch et al. 2003; Peng et al. 2004a).

Some of this work emphasized the use of three-band (two-color) photometry in order to reduce the contamination of the GC samples by foreground stars and background galaxies—a problem which can otherwise become severe at large radii and for the less luminous galaxies. This issue can be addressed even further by subarcsecond image quality, which resolves out many of the background contaminants. Deep exposures are also important to reach beyond the peak of the GC luminosity function and thereby to allow for proper GC number counts.

This critical combination of imaging attributes—wide-field, deep, good seeing, multi-color—has never before been carried out in a homogeneous survey of galaxies, but is now an integral part of both NGVS and SLUGGS. The main imaging source for SLUGGS is Suprime-Cam: the best instrument in the world for producing spatially complete GC system catalogs, owing to the telescope's 8 m aperture, the large areal coverage ($34' \times 27'$),

Figure 7. Three color (gri) Suprime-Cam image of NGC 4365, with its globular cluster (GC) candidates marked by small circles. This image is a zoom-in at $\sim 18' \times 17'$ ($\sim 120 \times 110$ kpc) of the original, which is three times the area. An *HST*/Advanced Camera for Surveys image mosaic was also used to select GCs out to $\sim 4'$ from the galactic center. Blom et al. (2012a) determined that NGC 4365 has 6450 ± 110 GCs and that its GC system extends beyond 9.5 galaxy effective radii.

(A color version of this figure is available in the online journal.)

and the typically excellent seeing on Mauna Kea. Most of the data are taken explicitly for our survey, although some of the images are found in the SMOKA archive (Baba et al. 2002). For a few of the galaxies, we make use of archival data from Canada–France–Hawaii Telescope/MegaCam (Boulade et al. 2003). In almost all cases these wide-field data are supplemented with *HST* imaging of the galaxy centers (see Section 3.1.3).

3.1.2. Imaging Acquisition and Reduction

Imaging is carried out in three filters for each galaxy: g, r and i (except for a few galaxies with adequate archival data available). Our nominal target for each filter is S/N ~ 20 at one magnitude fainter than the turnover of the GC luminosity function (occurring at $M_i \sim -8$). The total exposure times depend on the band, galaxy distance, and observing conditions, ranging from ~ 300 s for the r-band in the nearest galaxies in the sample, up to ~ 4000 s for the g-band in the most distant. We use a five-point dither pattern to fill in the chip gaps. We also take very brief, ~ 10 s exposures in order to obtain unsaturated images of the galaxy centers and of any bright UCDs.

Our reduction of Suprime-Cam imaging is largely based on the SDFRED package (Yagi et al. 2002; Ouchi et al. 2004),

but incorporates custom modifications to improve the sky subtraction and alignment of images. High-quality astrometric solutions across the Suprime-Cam field of view are essential for spectroscopic follow up. In order of preference, astrometric calibration is linked to the SDSS DR7 (Abazajian et al. 2009), USNO-B2 (Monet et al. 2003), or 2MASS (Skrutskie et al. 2006), with typical rms values of $\sim 0''.15$. An example of a reduced Suprime-Cam image is provided in Figure 7.

3.1.3. Globular Cluster Photometry and Selection

Object detection and photometry are performed using the DAOPHOT suite (Stetson 1992). All photometry is aperture photometry, using optimal extraction radii and aperture corrections calculated for each set of images. Photometric calibration is achieved using standards taken during the run, or by reference to point sources in SDSS DR7. Corrections for foreground dust extinction are applied using standard maps (Schlegel et al. 1998).

Significantly extended objects are removed as probable background galaxies (slightly resolved objects could be UCDs and are not excluded). The GC sequence is defined in $g-i$ versus $r-i$ color–color space (see example in Figure 8 and cf. Sinnott
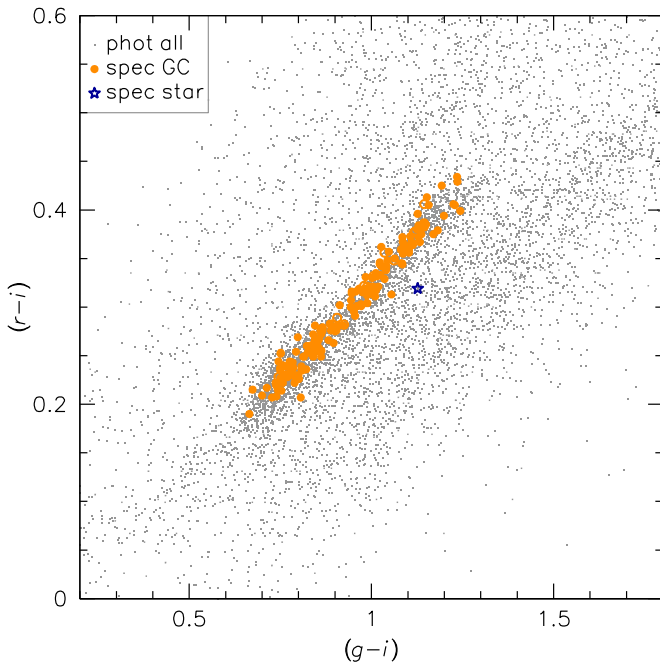
Figure 8. Color–color diagram ($r-i$ vs. $g-i$) for GCs in NCC 1407. All objects in the Suprime-Cam field are given as gray points. Objects with spectroscopic identification (Romanowsky et al. 2009) are shown with larger colored symbols: GCs (orange circles) and a star (blue star symbol). With deep, high-quality imaging and three-band selection, we achieved <1% contamination levels in our spectroscopic sample. Some other galaxies in our sample have sparser GC systems and shallower imaging data, so the results are not as good.

(A color version of this figure is available in the online journal.)

et al. 2010). This sequence is fairly well-separated from the foreground-star sequence, except at the bluest end (where near-infrared imaging would help in principle; Muñoz et al. 2014). We thereby obtain a sample of GC candidates that is relatively contaminant-free, as is important both for spectroscopic target selection, and for general photometric studies of the GC systems. The bright magnitude GC selection limit is set by the expected range of UCDs (up to $M_i \sim -13$; Brodie et al. 2011); the faint limit varies according to the actual depth of the imaging.

Detection, secure identification, and photometric analysis of GCs from ground-based imaging become challenging near the centers of bright galaxies. Fortunately, almost all of the SLUGGS galaxies have archival imaging available from *HST*, allowing for improved GC detection and photometry closer to the galactic centers. The *HST* analysis is similar to that for ground-based imaging, although only one color is typically available (see Spitler et al. 2006; Strader et al. 2006). The principal difference is that the vast majority of the GCs in our survey are resolvable by *HST*, which allows for another step in contaminant reduction (eliminating the foreground stars in the central regions of the galaxies). We also use information from *HST* to fine-tune the parameters used in the Suprime-Cam GC selection.

Once all of the data have been processed, full photometric catalogs and imaging data for the SLUGGS galaxies will be made publicly available on the project Web site.[9]

3.1.4. Galaxy Surface Photometry

Our wide-field imaging is also suitable for studying the host galaxy, although this is currently the least advanced aspect of

---

[9] http://sluggs.ucolick.org

our survey. Suprime-Cam is not optimally suited for mapping out the extended low surface brightness regions of galaxies, owing to limitations with flat-fielding and scattered light that are typical for most telescopes, and require special instrument configurations or heroic processing efforts to circumvent (e.g., Tal et al. 2009; Janowiecki et al. 2010; Paudel et al. 2013). However, our survey imaging still reaches fainter surface brightness levels than SDSS, which is important for studying the interesting outer regions of the galaxies.

Using the standard IRAF task ELLIPSE, we measure the isophotes in the annuli, thus building up a 2D description of the galaxy light (see Blom et al. 2012a). The resulting data include the radial profiles of surface brightness, ellipticity, position angle, and higher order Fourier components (such as boxiness and diskiness). These profiles are used throughout the survey in various contexts, such as in dynamical models, derivations of galaxy color profiles, and in comparisons of GC system properties (spatial and kinematical) to the diffuse galaxy light.

The extended stellar light can also be inspected for substructures produced by galaxy interactions and mergers. Although our sample was designed to avoid galaxies where such features are dominant, we have serendipitously discovered several halo substructures in our Suprime-Cam data.

Figure 9 shows one example, presented here for the first time. An S0 galaxy, NGC 4111, is seen to be linked by a faint tidal stream to a smaller spiral galaxy, UGC 7094 (=PGC 38375). The UGC 7094 stream has a maximum surface brightness of $\mu_g \sim 26.4$ mag arcsec^{-2}, spans an apparent length of ~ 75 kpc, has a slightly redder color than its parent galaxy, $(g-i)_0 \sim 0.93$ versus ~ 0.81, and a similar luminosity ($L_g \sim 2 \times 10^8 L_{g,\odot}$ versus $\sim 3 \times 10^8 L_{g,\odot}$).

The stream thus appears to represent an ongoing minor merger, with a stellar mass ratio of $\sim 1:20$ (based on *i*-band luminosities). Another S0 galaxy toward the north east, NGC 4117, shows distorted outer features (not shown in the figure), suggesting that we may be witnessing multiple interaction events happening within a small group of galaxies as it falls into the Virgo cluster.

The Suprime-Cam imaging also allows us to do far more than characterize substructures photometrically; we can identify embedded GCs for spectroscopic follow up with DEIMOS, allowing the chemodynamics of the features to be explored. So far, we have used this approach for stellar streams around two galaxies in the survey, M87 and NGC 4365 (Romanowsky et al. 2012; Blom et al. 2014). These data allowed us to identify, for the first time, NGC 4342 as the origin of a stream in the NGC 4365 system.

The number of discrete spectroscopic tracers in substructure can be increased beyond GCs by acquiring supplementary narrow-band imaging with Suprime-Cam to identify PNe, which we then follow up with DEIMOS (Foster et al. 2014).

3.2. Spectroscopy

3.2.1. DEIMOS Mask Design and Observations

Our default strategy for spectroscopy is to obtain four $15' \times 6'$ Keck/DEIMOS slitmasks for each galaxy in a "hub and spoke" layout (see Figure 3 of Arnold et al. 2014). This arrangement provides good radial and azimuthal coverage while allowing for mask overlap in the densely populated central regions of the galaxy. In galaxies with especially sparse or populous GC systems, this default of four masks is sometimes adjusted.
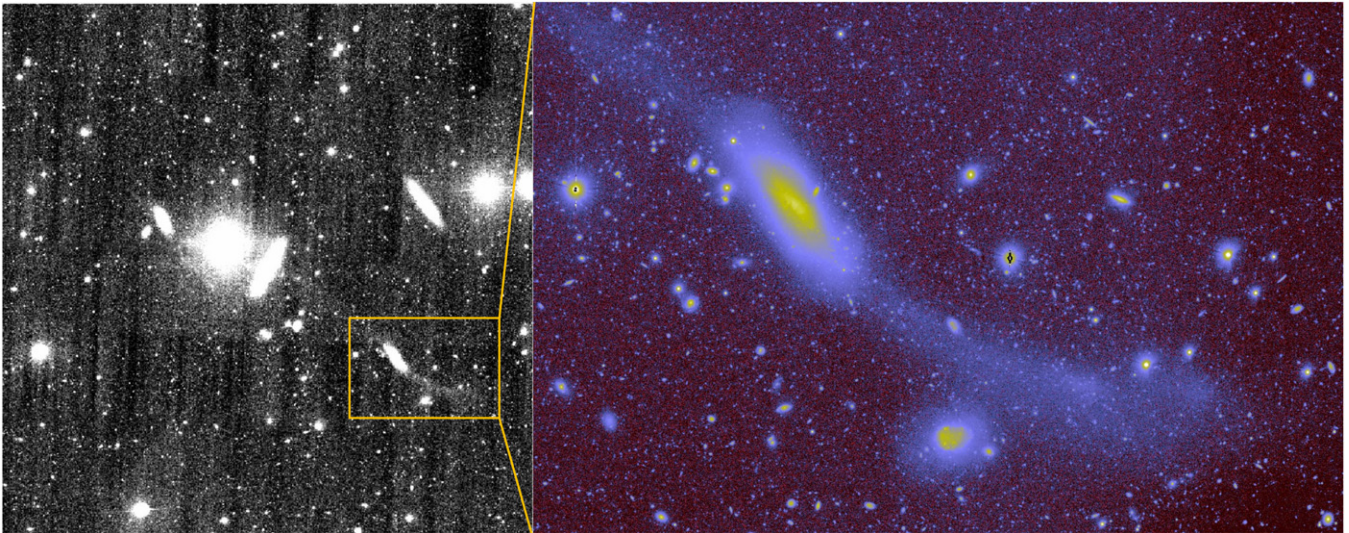
Figure 9. Illustration of the power of Suprime-Cam for studying diffuse stellar substructures. The left panel shows an SDSS image, courtesy of Tomer Tal, composed of stacked g, r, and i bands and centered on the low-luminosity S0 galaxy, NGC 4111. North is up, east is left (the bright object to its north east is a foreground star). There is a faint indication of a previously unreported stellar stream extending out to the southwest through a smaller spiral galaxy. The area in the box is shown in the right panel with g filter imaging from Suprime-Cam (with false color used to enhance the image contrast). Compared to SDSS, the Suprime-Cam imaging has greater depth and resolution, making it possible to analyze the luminosity and detailed structure of the stellar stream, and to do spectroscopic follow up of discrete tracers within it.
(A color version of this figure is available in the online journal.)

Candidates are selected to maximize the number of high-S/N GC spectra per mask. Objects down to $i \sim 23$ are targeted (corresponding to $M_i \sim -8$ for a reference galaxy at the distance of the Virgo Cluster). Any unused mask "real estate" is then devoted to "filler" slits (generally centered on random objects) used to measure both sky background and galaxy light (see Section 3.2.3 below). Typically 50–150 candidates are observed per mask, depending on the mask position and GC system richness. Each mask is observed for 1.5–2.5 hr in individual exposures of 30 minutes. The total observing time is adjusted depending on the prevailing seeing and transparency conditions.

The observations are made with DEIMOS configured with a 1200 line mm^{-1} grating centered on 7800 Å. The width of the mask slits is 1″, which implies an average FHWM resolution of ∼1.6 Å. This setting provides wavelength coverage of the region ∼6500–9100 Å.

3.2.2. Globular Cluster Spectroscopy

The DEIMOS GC spectra are reduced using the `spec2d` pipeline (Cooper et al. 2012; Newman et al. 2013b), which provides flat fielding, wavelength calibration, sky subtraction, and optimized spectral extraction.

Radial velocities are determined through cross-correlation with a library of stellar templates observed with the same instrument and set-up, using the region of the CaT at 8498 Å, 8542 Å, and 8662 Å. Visual identification of at least two clean lines (usually CaT lines, but sometimes including Hα), by at least two independent observers, is required to confirm the velocity. Uncertainties are determined using the width of the cross-correlation peak and the variance among stellar templates, with a minimum uncertainty of 5 km s^{-1} (enforced) and a median value of ∼12 km s^{-1} (determined from the 21 galaxies analyzed so far). Our uncertainties have been verified by repeated measurements over a large range in S/N, which is part of a general framework of redundancy in our program, designed to prioritize quality control along with sheer quantity of GC velocities.

We note that for a few galaxies, we supplement the spectroscopic coverage with data from other telescopes or instruments (e.g., Keck/LRIS; MMT/Hectospec; Magellan/IMACS). These additions are discussed in the relevant papers (e.g., Arnold et al. 2011; Strader et al. 2011). Having occasional spectroscopic targets in common between DEIMOS and other instruments, and between multiple DEIMOS observations, allows us to monitor our results for reproducibility. As discussed previously (Romanowsky et al. 2009; Strader et al. 2011; Pota et al. 2013), such comparisons demonstrate extremely good consistency for the DEIMOS velocities. However, a few objects in common with the literature show catastrophically large discrepancies, at up to 10σ difference, which may be attributable to marginal S/N in the older measurements. As discussed in Strader et al. (2011), even a few such outliers can change the kinematic inferences enormously, which further motivates the strict quality control that we have adopted in our survey.

In typical seeing of 0″8, radial velocities are measurable with DEIMOS for a good fraction of the faintest ($i \sim 23$) GC candidates in each mask. The GC return rate per mask depends upon a number of factors, such as the seeing, the intrinsic richness of the GC system, the galactocentric distance of the mask, and the photometric GC selection criteria. In the best cases, where the galaxy has a populous GC system and imaging data are available from both *HST* and Subaru, a single mask can return up to 60–70 GCs. The radial extent of the GC velocities, based on the 12 galaxies analyzed to date (Pota et al. 2013), is typically 8 R_e, and in some cases up to 15 R_e.

Background galaxies can often be identified by the presence of emission lines in their spectra. By contrast, foreground G and K stars have spectra that are very similar to those of GCs. In some cases their velocities are sufficient to identify these objects as stars. In rare cases the systemic velocity of the targeted galaxy is low enough that there is potential overlap between the velocity distributions of Milky Way stars and target galaxy GCs. No universal criteria are used for GC discrimination in these galaxies; uncertain objects have been flagged in the

appropriate catalogs and additional discussion is present in the corresponding papers when necessary.

In addition to kinematics, DEIMOS spectra are used to obtain GC metallicities based on the CaT index, which is a measure of the strength of the Calcium II triplet absorption lines at 8498, 8542, and 8662 Å, relative to the local continuum; the precise definition of the index may be found in Usher et al. (2012). Unfortunately, the CaT is in a region of the spectrum containing several strong sky emission lines that make line index measurements difficult for faint objects, such as distant GCs. We use a technique described in Foster et al. (2010, see also Usher et al. 2012) to reduce the effect of these sky lines on the CaT index measurement. We mask the sky line regions and fit a linear combination of stellar template spectra (the same templates used to measure the radial velocity). Each fitted spectrum is then continuum-normalized, and the strength of the CaT index is measured on the normalized spectrum. A Monte Carlo resampling technique is used to derive asymmetric confidence intervals for each index measurement. A number of weaker lines of Fe, Mg, Ti, Na, and other elements are present in the GC spectra, and their strengths can be measured once spectral stacking has increased the S/N (see Section 5.2 and Figure 16; Usher et al. 2014).

3.2.3. Stellar Spectroscopy

The spec2d reduction pipeline generates the subtracted background spectra (loosely referred to as "sky"). However, because our point-like targets are projected onto the host galaxy, these background spectra are a combination of pure sky and galaxy background light. We use the SKiMS technique (Norris et al. 2008; Proctor et al. 2009; Foster et al. 2009; Schuberth et al. 2012; Richtler et al. 2014) to extract the galaxy spectrum from these background spectra. Briefly, we use a specially defined "sky index" to identify pure-sky slits at large galactocentric distances (typically 6–7 R_e), where the contribution of galaxy light is insignificant.

In earlier SLUGGS work, the pure-sky spectra were co-added and normalized into a single master sky spectrum that was then scaled for non-local sky subtraction for each slit (Proctor et al. 2009; Foster et al. 2009, 2011). In order to minimize the impact of small variations of the spectral resolution across the spatial axis of the DEIMOS mask, in recent SLUGGS work we have used the penalized Pixel Cross-correlation Fitting (pPXF) routine by Cappellari & Emsellem (2004) to derive a linear combination of pure-sky spectra that best matches the sky component in each slit (see Arnold et al. 2014).

This sky spectrum, individually optimized for each slit, is then subtracted from the corresponding slit, and the remaining signal is the galaxy stellar-light spectrum. Because these SKiMS spectra are spread in two dimensions around the galaxy, in accordance with the GC targets, we can thereby effectively use DEIMOS as a sparsely sampled integral-field unit.

This method yields a final continuum level in the sky index definition region accurate to <1% of the noise in the skyline residuals (see Foster et al. 2009). As an example, Figure 10 illustrates the sky index definition and sky-subtracted spectrum for the galaxy light of NGC 4494. Using this procedure, we obtain galaxy spectra that typically extend to 2–3 R_e, with some reaching 4 R_e.

Stellar kinematics are measured using pPXF. Briefly, the code uses the fully propagated variance array to proportionally "penalize" pixels in the spectrum. Template spectra are convolved with Gauss–Hermite polynomials and compared to
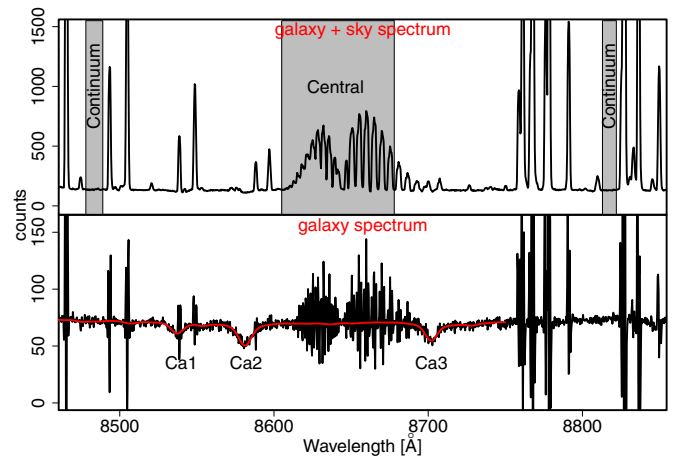

Figure 10. Example of a typical DEIMOS spectrum of galaxy light, before (top panel) and after sky subtraction (lower panel), for NGC 4494 at ∼1 R_e, a location where the surface brightness is $\mu_i = 21.4$ mag arcsec^{-2}. The pPXF template fit is shown in red. The passbands of the sky index are highlighted in gray in the original spectrum (see text) and the positions of the redshifted CaT features are labeled on the subtracted spectrum.

(A color version of this figure is available in the online journal.)

the observed spectra. The routine identifies the set of kinematic parameters and templates that minimizes residuals between the observed and combined template spectrum. We simultaneously fit the first four velocity moments (i.e., recession velocity, velocity dispersion, higher-order Gauss–Hermite moments h_3 and h_4). Uncertainties are measured using Monte Carlo methods. Our kinematic measurements are described in detail in Arnold et al. (2014). Figure 10 shows an example SKiMS spectrum together with its best fit pPXF output template spectrum.

For the highest S/N spectra, we measure the strength of the CaT index for the diffuse stellar light to large radii using the technique described in Foster et al. (2009). The index is the weighted sum of the equivalent width of all three CaT lines. A correction is applied to account for the velocity dispersion broadening. CaT indices are then converted into metallicity as described in Section 4.2.3. In this manner, we are able to generate metallicity maps out to typically ∼1.5–2 R_e, with some reaching 3 R_e (not quite as far as the kinematics measurements owing to the greater S/N requirements; for more detail, see Foster et al. 2009, 2011; Pastorello et al. 2014).

4. MODELING

Here we describe various methods for modeling the observational measurements from Section 3 and thereby converting them into products of more direct scientific interest, such as maps of stellar velocities, mass profiles, etc.

4.1. Globular Clusters

4.1.1. GC Numbers and Spatial Distributions

Accurate GC number counts, including reliable uncertainties, are important for interpretations of their formation histories (e.g., Bekki et al. 2008; Coenda et al. 2009), estimates of stellar halo masses (Brodie & Strader 2006), and for analyses of their correlations with interesting galaxy properties such as supermassive black hole masses and dark matter halos (e.g., Spitler & Forbes 2009; Burkert & Tremaine 2010; Harris & Harris 2011; Snyder et al. 2011; Rhode 2012; Harris et al. 2013,

2014; Wu & Kroupa 2013; Forte et al. 2014; Durrell et al. 2014). One of the goals of the SLUGGS survey is to provide an updated set of reliable GC numbers (including the red and blue subpopulations separately), and then to explore what impact these have on the scaling relations. As described below, some of the literature values of N_{GC} are in error by factors of three or more, and we anticipate that our more accurate estimates will clarify these fundamental relations.

Although every care is taken to ensure the GC catalogs from photometric data contain very little contamination (from foreground stars and background galaxies; see Section 3.1.3), a certain amount is unavoidable and will impact measurements of the true GC number counts. Fortunately, the contaminants contribute a fairly constant surface number density over the regions covered by the GC systems. This surface density is typically estimated as a free parameter in fits to the GC surface density profiles, and can be cross-checked via spectroscopic contamination rates (Strader et al. 2011; Usher et al. 2013).

To derive total GC numbers around a galaxy, the surface density profile is integrated with the radius. Correction must also be made for the fraction of GCs that were too faint to be included in the catalogs. Since the functional form of the GC system luminosity function is predictable (Jordán et al. 2007), the missed GCs can be accounted for by measuring the brighter parts of the luminosity function and extrapolating to faint magnitudes (which can be done securely because the SLUGGS images are designed to reach past the turnover luminosity). Corrections are thus made for completeness and contamination as a function of magnitude.

As an illustration of the importance of reliable surface density distributions for deriving accurate estimates of N_{GC}, Figure 11 shows the surface density and cumulative number profiles of blue and red GCs with radius around NGC 1407, based on Suprime-Cam imaging. The cumulative profiles flatten out at a radius of ∼14 arcmin (∼110 kpc), corresponding to the edge of the Suprime-Cam image. Thus, with very high quality, wide-field imaging, one can just barely get a reliable count of total GC numbers around a high-mass elliptical galaxy at 27 Mpc.

For poorer-quality data, narrower fields, or more nearby massive galaxies, the total GC counts can become precarious. For NGC 1407, a single *HST*/Advanced Camera for Surveys (ACS) pointing picks up only ∼10% of the total GCs (Forbes et al. 2006), and ground-based imagers with ∼10–20 arcmin fields would subtend only half of them. Naturally such limitations are obvious, and attention has been given in the literature to making reasonable extrapolations while accounting for the associated uncertainties, but the results until now have not been encouraging. As a case in point, the giant elliptical NGC 4365 was analyzed with a central ACS pointing supplemented by parallel WFPC2 imaging, and estimated to have 3246 ± 598 GCs by Peng et al. (2008). Our subsequent analysis of Suprime-Cam imaging found a lower-limit of 6450 ± 110 GCs (Blom et al. 2012b), which is higher than the previous result by at least 5σ.

Besides total numbers, our Subaru data allow accurate surface density distributions to be derived for the SLUGGS galaxies out to large radii. We can improve on past procedures for determining important basic parameters for these galaxies, such as R_e, by fitting Sérsic models both to the galaxies and to their GC systems (see, e.g., Blom et al. 2012b; Usher et al. 2013; Kartha et al. 2014, for GCs).

On a related note, the analysis of the radial "extent" of GC systems (e.g., Rhode et al. 2007) is also sensitive to limitations with the imaging data. For example, analysis of the SLUGGS
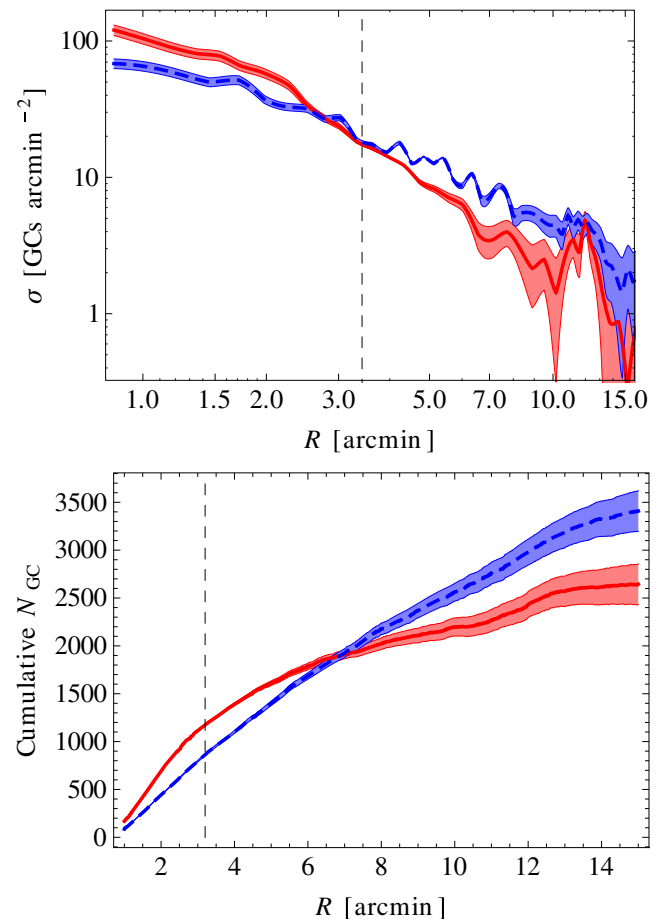

Figure 11. Radial distribution of GCs around NGC 1407, with the blue and red GC subpopulations shown as dashed blue and solid red curves, respectively. In both panels, the shaded areas show the 1σ uncertainty regions, including both Poisson errors and the uncertainties in the contamination levels (which have been subtracted from the profiles). Top panel: interpolated surface density profiles with radius on a logarithmic scale. Bottom panel: cumulative numbers versus radius on a linear scale. For simplicity, no attempt has been made to mask out the contributions from the smaller companion galaxy, NGC 1400, which produces the bump in the red GC profile starting at ∼12 arcmin. The vertical dashed line marks the limits of the (off-center) *HST*/ACS field-of-view. The GCs are selected over the magnitude range of $i = 20.6$–25.5, with no correction applied for incompleteness over the luminosity function, so the numbers here are relative, not absolute. The profiles are terminated when the annuli reach the edges of the field, at about 15 arcmin. The cumulative profiles begin to level off at this radius, allowing for reasonably reliable estimates of the total GC numbers by using the wide-field Suprime-Cam imaging. The red GC system is more centrally concentrated, whereas the blue GC system is more radially extended, as found for most massive galaxies.

(A color version of this figure is available in the online journal.)

data for NGC 720 by Kartha et al. (2014) revealed that its GC system extent had previously been underestimated by a factor of three.

4.1.2. GC Kinematics

The kinematics of a GC system can be characterized by the rotation amplitude v_{rot} along a position angle θ_0, and by the rotation-subtracted velocity dispersion σ_p. These parameters quantify the amounts of coherent rotation and random motion of the system, and they can be compared to the same quantities for stellar kinematics. We study these quantities using a maximum-likelihood approach (Kissler-Patig & Gebhardt 1998) that we have extended to allow for flattened galaxies (see details in Pota et al. 2013 and discussion in Romanowsky et al. 2009 about
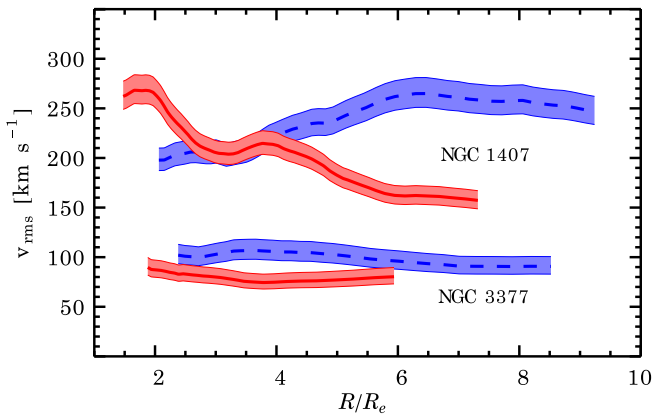
Figure 12. GC system rms velocities vs. galactocentric radius, normalized by the galaxy effective radius, for NGC 1407 (top curves) and NGC 3377 (bottom curves). Dashed blue and solid red curves correspond to the blue and red GC subpopulations separately. Uncertainties are indicated by shaded regions. The radii have been circularized to account for galaxy ellipticity (see Pota et al. 2013). The blue and red GCs show kinematical differences that reflect distinct spatial and orbital properties.

(A color version of this figure is available in the online journal.)

problems with other methods). The approach is equivalent to a simplified version of kinematry used for galaxy stellar-light kinematics (see Section 4.2.2).

One particular kinematic measurement of interest is the projected rms velocity v_{rms} which, as a metric of specific kinetic energy, can be connected through dynamical modeling to estimates of mass. Figure 12 shows v_{rms} profiles for two example SLUGGS galaxies, one high-mass (NGC 1407) and one low-mass (NGC 3377), using SLUGGS data from Pota et al. (2013). For each galaxy, the data are separated into profiles for the blue and red GC subpopulations. The case of NGC 3377 illustrates the generic result that the blue GCs have higher rms velocities than the red GCs, as expected from the larger spatial extent of the blue GC system density profile (which must be supported by hotter kinematics in the same gravitational potential). In some cases like NGC 1407, the radial behaviors of the v_{rms} profiles are also different, which probably reflects very different orbital types between the blue and red GCs.

Interpreting these kinematic data through dynamics, in terms of orbital properties and mass profiles, will be discussed further in Section 4.3. It should be noted however that the observed v_{rms} profiles are not generally smooth, which is a complication that should ultimately be addressed by allowing for strong orbital variations in the models. In addition, some of the observed fluctuations may be produced by substructures, thereby providing valuable clues about recent merging events (cf. Romanowsky et al. 2012; Coccato et al. 2013; Schauer et al. 2014; Murphy et al. 2014).

4.1.3. GC Metallicities

The metallicities of the GCs are derived using the CaT index (Section 3.2.2), whose strength has previously been shown to be sensitive to changes in mean metallicity (Armandroff & Zinn 1988; Diaz et al. 1989; Cenarro et al. 2001; Foster et al. 2009, 2010). CaT is independent of age for stellar populations older than 3 Gyr (Vazdekis et al. 2003). Although the index is sensitive to a bottom heavy initial mass function (IMF; Vazdekis et al. 2003), our CaT measurements are insensitive to horizontal branch morphology and to α element enhancement (Brodie et al. 2012).

We have compared CaT metallicities with literature values derived using traditional Lick Index analyses, finding excellent agreement between the two techniques (with a reduced χ^2 value of 0.59; Usher et al. 2012). We use the single stellar population models of Vazdekis et al. (2003) to derive the following relation for converting the CaT index strengths into metallicities:

$$[Z/H] = (0.461 \pm 0.013)\,\mathrm{CaT} + (-3.750 \pm 0.080)\,. \quad (1)$$

Further details of the CaT metallicity measurement techniques are given in Usher et al. (2012).

4.2. Galaxy Starlight

4.2.1. Stellar Density Distributions

As for the GC density distributions (Section 4.1.1), the stellar densities are needed for dynamical models, after converting the raw density profiles derived from the images (Section 3.1.4) into parameterized forms such as the Sérsic (1968) law. The photometry can also be analyzed to derive estimates of galaxy luminosity, effective radius, etc.—basic quantities which, as discussed in Section 2 and in the Appendix, are reliably and homogeneously available for our sample. Details of the galaxy photometry and results will be reported in future papers.

4.2.2. Stellar Kinematics

Once the SKiMS-based stellar kinematics measurements are obtained (Section 3.2.3), the overall kinematic structure of the galaxy can be visualized through 2D maps. Several methods have been used for preparing these maps, including Voronoi binning with semi-variogram-based smoothing (Arnold et al. 2014), and kriging interpolation (Krige 1951; Matheron 1963; Cressie 1988; Foster et al. 2013). An example of the latter is shown by Figure 13.

As with the GCs (Section 4.1.2), the full 2D kinematical information for the stellar light can be reduced to one-dimensional profiles through modeling. We adopt a "kinemetry" approach, originally designed by Krajnović et al. (2006) for IFU data-cubes, and extended to sparsely sampled data by Proctor et al. (2009) and Foster et al. (2011). Kinemetry is analogous to ellipse-based galaxy surface photometry and assumes that the rotation and the dispersion are stratified on ellipses. These profiles generally include the rotation amplitude, position angle, and "flattening" or ellipticity (which is often, but not always, similar to the photometric ellipticity; cf. Krajnović et al. 2008). The kinemetry results for the survey will be presented in Foster et al. (2015).

4.2.3. Stellar Metallicities

As discussed in Section 3.2.3, CaT indices can be measured for the integrated starlight out to radii of typically $\sim$1.5–2 R_e. These values are converted to total metallicities [Z/H] using Equation (1), but with an empirical correction that takes into account the observed dependence of CaT-derived metallicities on galaxy mass. Pastorello et al. (2014) suggested that this dependence may be a reflection of the index's sensitivity to the slope of the IMF, and derived the correction by comparing our values to metallicities from overlapping SAURON data (Kuntschner et al. 2010).

The uncertainties are evaluated using Monte Carlo resampling of the spectra, in a method similar to the one adopted for GC metallicities (Section 4.1.3).

In order to obtain smooth 2D stellar metallicity maps for the galaxies in our sample, we interpolate between our data points
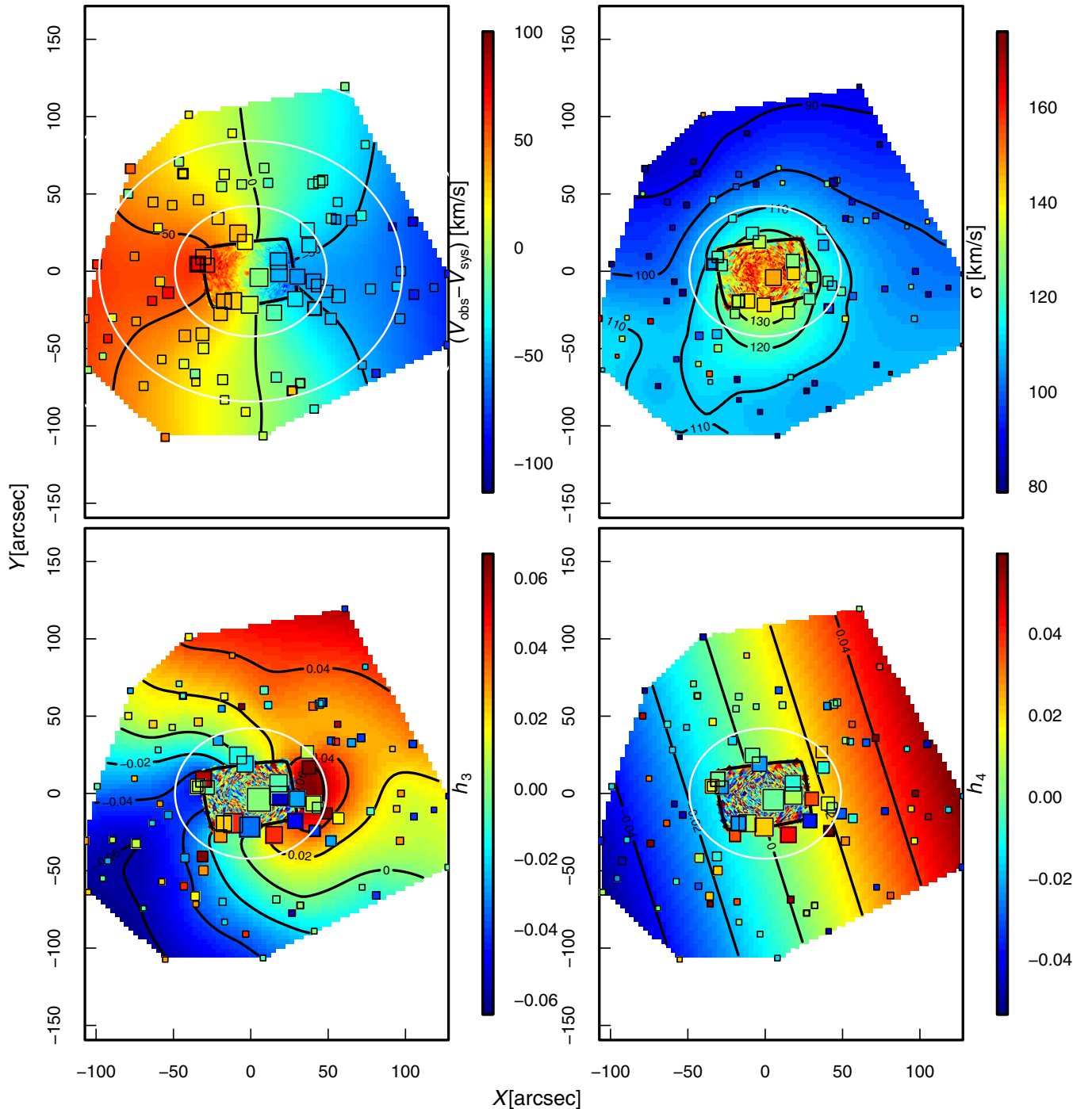
Figure 13. Example 2D stellar kinematic maps for the elliptical galaxy NGC 4494: recession velocity (upper left), velocity dispersion (upper right), third-order (h_3, lower left) and fourth-order (h_4, lower right) Gauss–Hermite velocity moments. Filled squares show individual SKiMS data points (Foster et al. 2011), with sizes proportional to spectral signal-to-noise. The smooth color mapping and iso-moment contours (black) are derived using kriging to fit the underlying 2D field (see, e.g., Foster et al. 2013; Pastorello et al. 2014; the color scale is provided to the right of each panel, and the contours are labeled). White ellipses in all panels show the photometric effective radius (R_e), with the upper left panel also including the $2 R_e$ ellipse. These maps join smoothly to the SAURON/ATLAS[3D] data from the central regions (shown within rectangles), but as in Figure 3 show novel features in the outer regions, including a surprising degree of flattening for the outer mean velocity field (which is not traced by the very round isophotes).

(A color version of this figure is available in the online journal.)

with the kriging technique (Pastorello et al. 2014). An example of a 2D stellar metallicity map derived in this way is shown in Figure 14 for NGC 4111.

From these 2D maps we extract azimuthally averaged radial metallicity profiles, from which we measure the inner ($R < 1 R_e$) and outer ($R > 1 R_e$) metallicity gradients. These gradients are powerful tools for constraining galaxy formation models and

feedback processes (e.g., Mihos et al. 2013; Hirschmann et al. 2015). For example, galaxies with more active merger histories should have fairly flat metallicity profiles at large radii (White 1980), while galaxies dominated by in situ star formation should have steep gradients, with their chemical enrichment being dependent on the distance from the center of the gravitational potential.
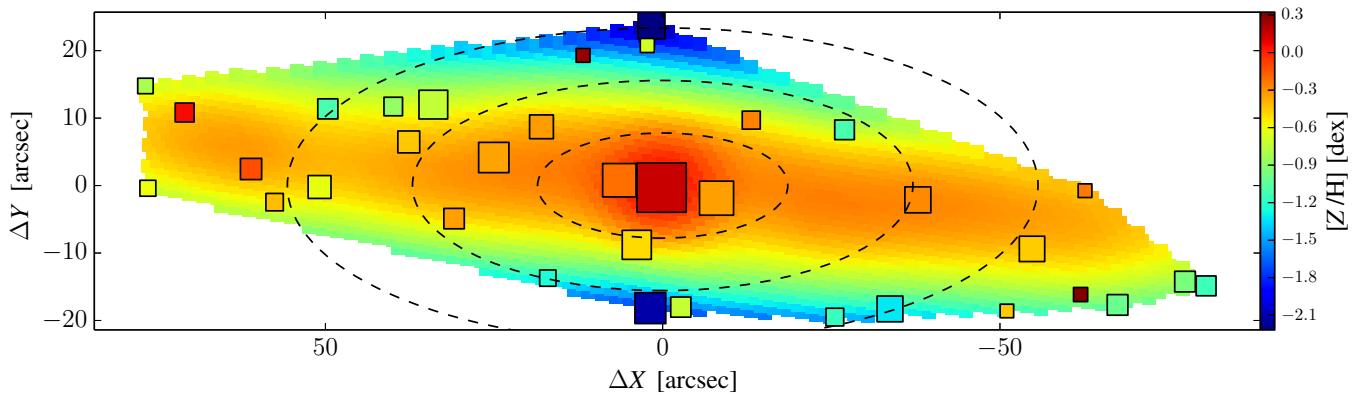
Figure 14. NGC 4111 stellar metallicity map (where *X* is the galaxy major axis and *Y* is the minor axis). The square symbols show the SKiMS metallicity values, color coded according to their metallicity (see scale bar at right) and with the size inversely proportional to the associated uncertainty. The pixel values are obtained via kriging interpolation of the SKiMS points and are color coded according to the same metallicity scale. From the center to the outskirts, the dashed lines present the galaxy isophotes with circularized radius $R = 1, 2, 3 R_e$. The coordinates on the axes are relative to the center of the galaxy. An extended metal-rich disk is apparent from this map (note that the slight tilt of the disk is an artifact of the incomplete spatial sampling). A strong negative metallicity gradient emerges along the minor axis.

(A color version of this figure is available in the online journal.)

4.3. Galaxy Dynamics and Masses

One of the main science drivers for SLUGGS is to use stars and GCs as dynamical tracers in the outer regions of ETGs and thereby to map out their dark matter halos, since H I rotation curves are not generally available in these galaxies. Although this approach, along with the use of PNe, has been pursued for decades, robust conclusions have remained elusive. This is in part because of modeling uncertainties and degeneracies (e.g., de Lorenzi et al. 2009), but also because the lack of a large sample of galaxies with homogeneous data has limited the statistical weight of the conclusions.

Furthermore, the galaxies previously well-studied with GC dynamics were limited to the high-luminosity ellipticals at the centers of galaxy groups and clusters, while it is only with the advent of more efficient spectroscopy that the realm of $\sim L^*$ early-types can be investigated properly (see Figure 6). This is an important area of parameter space not only because such galaxies are more "ordinary" and allow for fairer comparisons with $\sim L^*$ spirals such as the Milky Way (e.g., Trujillo-Gomez et al. 2011), but also because of reports based on PNe that the mass profiles of these galaxies are systematically different from those of the brightest ellipticals, with much less dominant dark matter halos (Romanowsky et al. 2003; Napolitano et al. 2011; Deason et al. 2012).

In order to focus the discussion about the limitations and opportunities for dynamical modeling, we construct a set of toy galaxy models and present the circular velocity and projected velocity dispersion profiles in Figure 15. These models consist of spherical ETGs, with either $4 L^*$ or L^* luminosities, typical GC systems, and either standard Λ cold dark matter (ΛCDM) halos (Navarro et al. 1997)[10] or dark matter halos with

constant-density cores,[11] as might arise either from baryonic effects or from alternative types of nonbaryonic dark matter (see discussion in Newman et al. 2013a).

The top panel of Figure 15 illustrates some aspects of the mass distribution that may be learned through dynamical constraints that extend from the centers of galaxies to their outer parts, as in SLUGGS. Within the central few kpc of the galaxy, the circular velocity profile is hardly affected by large variations in the dark matter halo properties. This is because the stars dominate the central regions, which is an advantage for constraining the stellar mass (and IMF) using detailed data and models in these regions, but a disadvantage for learning about the dark matter distribution (e.g., Treu et al. 2010; Tortora et al. 2010; Cappellari et al. 2012).

It is clearly important to employ data extending to larger radii to constrain the dark matter halos. Here our SKiMS data have great potential, owing to their 2D coverage out to $\sim 3 R_e$ (~ 10 kpc), where the dark matter fraction is expected to be around 50%. These data, combined with central kinematics from SAURON/ATLAS^{3D}, may provide a unique opportunity to measure the slope of the central dark matter profile—which has so far been determined for dwarf, spiral, and brightest cluster galaxies (e.g., Oh et al. 2011; Chemin et al. 2011; Walker & Peñarrubia 2011; Newman et al. 2013a).

The GC kinematics data extend even farther out, to $\sim 8 R_e$ (tens of kpc), which is close to the expected dark matter halo scale radius. This is an important region to probe since it lies beyond the galaxy centers where myriad baryonic effects could have altered the dark matter profiles. At these large radii, it becomes possible to test the primordial mass–concentration relation that is a robust prediction of ΛCDM theory, at least for a given set of cosmological parameters (e.g., Dutton & Macciò 2014).

While the SLUGGS stellar and GC kinematics data sets are each expected to provide powerful constraints on their own, the full potential of the survey will be realized when all of the data are integrated into "global" dynamical models of the galaxies with large baselines in log-radius. In particular, each

---

[10] The $4 L^*$ galaxy has a stellar mass of $M_\star = 6.6 \times 10^{11} M_\odot$ and a Sérsic profile with index $n = 8$, and $R_e = 15$ kpc. The red GC system is assumed to follow the diffuse stellar light, and the blue GC system has $n = 4$ and $R_e = 50$ kpc. The dark matter halo in our default *Planck*-based cosmology has a scale radius of $r_s = 120$ kpc and a scale density of $\rho_s = 1.4 \times 10^6 M_\odot$ kpc^{-3} (corresponding to virial mass and concentration of $M_{200} = 3.6 \times 10^{13} M_\odot$ and $c_{200} = 4.5$; Dutton & Macciò 2014). The L^* galaxy has $M_\star = 7.2 \times 10^{10} M_\odot$, $n = 4$, and $R_e = 3.5$ kpc (for the stars), and $n = 4$ and $R_e = 6$ kpc for the blue GCs. The halo properties are $r_s = 48$ kpc and $\rho_s = 2.3 \times 10^6 M_\odot$ kpc^{-3} ($M_{200} = 4.6 \times 10^{12} M_\odot$ and $c_{200} = 7.1$). The velocity dispersions are calculated using the Jeans equations (Mamon & Łokas 2005). This L^* model is also used for the $M_{\rm tot}(r)$ profile in Figure 1.

[11] The cored model is based on a logarithmic dark matter potential as discussed in Thomas et al. (2009), with parameters $r_h = 5.0$ kpc and $v_h = 392$ km s^{-1} for the $4 L^*$ galaxy (following the scaling relation for old ETGs in the Coma cluster), and 3.5 pc and 200 km s^{-1} for the L^* galaxy (similar to the young ETGs).
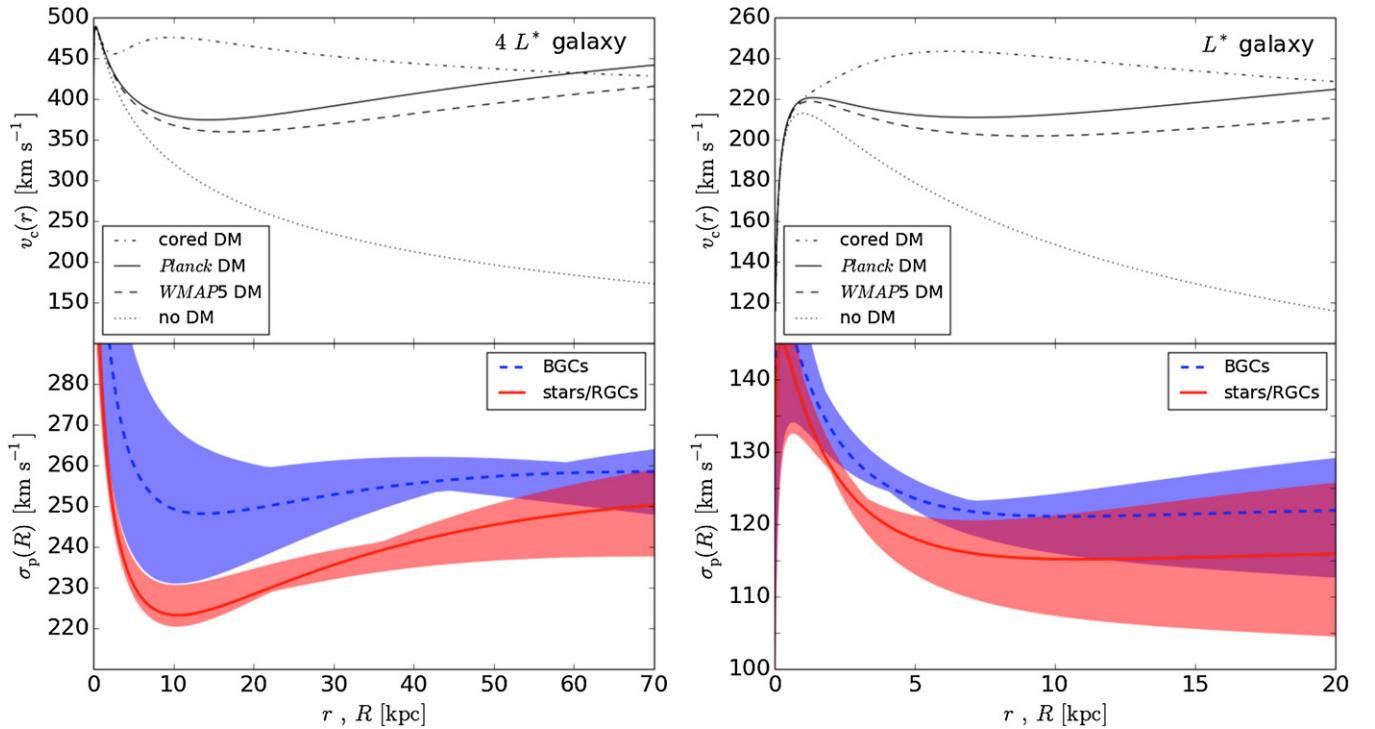
Figure 15. Schematic dynamical models for two elliptical galaxies, with $4\,L^*$ (left) and L^* (right) luminosities, showing radial profiles of circular velocity (top) and projected velocity dispersion (bottom). The circular velocities cover a range of models including no dark matter, as well as cored dark matter halos, and typical dark matter halos for different ΛCDM cosmological parameters (the latter systematic variation is similar to the galaxy-to-galaxy scatter for a fixed cosmology). These models are very similar inside a few kpc, and diverge at larger radii. The dispersion profiles are all calculated for the *Planck*-based model, with different assumptions on the velocity anisotropy, including isotropy ($\beta = 0$; central curves), tangentially biased ($\beta = -1$), radially biased ($\beta = +0.5$), and varying with radius from isotropic to radially biased (Mamon & Łokas 2005). The blue GCs and red GCs (or field stars) are shown separately, with dashed and solid curves, respectively. For a fixed anisotropy, the blue GCs have a higher velocity dispersion than the red GCs (cf. real data in Figure 12). For each subpopulation, there is a characteristic radius (the "pinch-point") where the dispersion profiles cross and the uncertainty from the anisotropy is minimized (cf. Agnello et al. 2014a; V. Pota et al., in preparation). The pinch-points for the more luminous galaxy extend deep into its dark matter halo, providing ample opportunities for model constraints, while the ordinary galaxy is more challenging to model definitively.

(A color version of this figure is available in the online journal.)

galaxy has between two and four tracer populations (stars and one, two or three GC subpopulations, depending on how many distinct subpopulations are present), each of them providing independent constraints on the mass profile for a distinct radial regime. This is an established approach for dwarf spheroidal galaxies with multiple stellar populations (e.g., Walker & Peñarrubia 2011; Amorisco et al. 2013), and can now be applied to GC systems with large data sets (Schuberth et al. 2010; Napolitano et al. 2014; Agnello et al. 2014b; V. Pota et al., in preparation).

Like GCs, PNe are also used as large-radius dynamical tracers. Here the approach is somewhat simpler because the spatial distribution of PNe can be assumed to follow the field starlight (see discussion in Courteau et al. 2014). However, GCs have the potent advantage of providing additional leverage through their subpopulations, with the blue GCs in particular extending to larger radii than the PNe (and red GCs; see bottom panels of Figure 15). Given the extensive overlap between SLUGGS and PN-studied galaxies (see Section 2) we plan to try incorporating joint GC and PN modeling constraints (cf. Forbes et al. 2012).

Most of our sample galaxies furthermore have detectable X-ray emitting hot gas halos (e.g., O'Sullivan et al. 2001; Boroson et al. 2011), some of which are suitable for mass analysis. We have started to compare optically based galaxy masses with those from X-rays and hence to test the assumptions inherent in both methods. So far we have found in two galaxies

that the mass estimates in the outer regions ($\sim$20–30 kpc) as derived from the hot gas were much greater than those from the GCs (and PNe; Romanowsky et al. 2009; Napolitano et al. 2014)—which presumably reflects departures from hydrostatic equilibrium. More generally, the mass estimates from the SLUGGS galaxies should prove useful in understanding the properties of the interstellar medium (e.g., Humphrey et al. 2013; Kim & Fabbiano 2013).

Given the above science goals and available data, there are a number of challenges for dynamical modeling. These include proper treatment of galaxy flattening, permitting and constraining orbital anisotropy, and uncertainties in the stellar mass (from IMF variations in particular). To tackle these issues, we are pursuing a layered modeling approach, ranging from simple mass estimators that may be applied quickly to many galaxies (Strader et al. 2011; Agnello et al. 2014a) to detailed, slower Schwarzschild-type orbit models (Romanowsky & Kochanek 2001; Gebhardt & Thomas 2009). We are also using techniques of intermediate complexity such as spherical Jeans models (Romanowsky et al. 2009; Napolitano et al. 2014), flattened Jeans models (M. Cappellari 2008, and in preparation), the projected virial theorem (Agnello et al. 2014b), and distribution function methods (Deason et al. 2012; Mamon et al. 2013). It should be noted that many of these mass-modeling methods are designed to simultaneously constrain the orbital anisotropy, e.g., by making use of higher-order information in the line-of-sight velocity distributions.

5. MAIN SCIENCE QUESTIONS AND EARLY RESULTS

Here we briefly summarize some highlights of the survey so far in the context of the scientific motivation outlined in Section 1, and indicate the directions of our future work. A complete list of SLUGGS papers to date can be found at our survey Web site.[12]

5.1. Evidence for Two-phase Galaxy Assembly

So far, the SLUGGS results support the dominance of a two-phase mode of galaxy assembly, as described in Section 1. The principal pieces of evidence include: broken radial metallicity gradients in the GC subpopulations (Arnold et al. 2011; Forbes et al. 2011), distinct core and halo kinematic behaviors of both the GCs and the underlying starlight (Arnold et al. 2011, 2014; Pota et al. 2013; Foster et al. 2013), and the presence of stellar streams, kinematical and positional fluctuations, and cold substructures in phase space (Romanowsky et al. 2012; Blom et al. 2014; see also Figure 9 and Section 4.1.2, as well as references in Section 1 and other GC-based results in the literature from Côté et al. 2003; Schuberth et al. 2010; Woodley & Harris 2011; D'Abrusco et al. 2014). Rotation is found to be relatively weak in the outer regions, at odds with general expectations for major mergers, but consonant with multiple, minor mergers in a cosmological context (Vitvitska et al. 2002; Bekki et al. 2008; Romanowsky & Fall 2012; Pota et al. 2013). Note that one rough prediction from cosmological accretion rates is that around half of nearby massive galaxies should have residual substructure in their GC systems from minor mergers (Figure 1).[13]

Despite this general agreement between observation and theory, there is a lingering puzzle about orbital anisotropy in the galaxy halos. Almost any model of spheroidal galaxy formation (monolithic collapse, major mergers, multiple minor mergers) predicts radially biased orbits as a relic of the infall of gas and stars (e.g., Dekel et al. 2005; McMillan et al. 2007; Oñorbe et al. 2007; Sales et al. 2007; Prieto & Gnedin 2008). In the context of two-phase assembly, the radial bias should be prevalent especially in the most massive ellipticals, where the ratio of accreted to in situ stars and GCs is the highest (Wu et al. 2014). However, there are long-standing indications that the orbits of GCs around both the Milky Way and giant ellipticals are near-isotropic or even tangentially biased (Frenk & White 1980; Romanowsky & Kochanek 2001; Côté et al. 2001; Hwang et al. 2008)—a result which has only strengthened with the advent of data from SLUGGS (Romanowsky et al. 2009; Deason et al. 2012; Spitler et al. 2012; Pota et al. 2013; Agnello et al. 2014b; K. A. Woodley et al., in preparation).

This observation has at times been attributed to a natural selection effect wherein GCs on near-radial orbits have been disrupted from passing close to the galactic center. However, this effect has not been shown to operate in the outer halos where low anisotropy is found (cf. Baumgardt 1998; Fall & Zhang 2001; Vesperini et al. 2003; Brockamp et al. 2014). The only other explanation so far proposed is preferential orbit dragging during

galaxy formation by slow accretion and adiabatic contraction (Agnello et al. 2014b).

5.2. Distinct Subpopulations in GC Systems

For over two decades it has been realized that most massive galaxies possess GC systems with bimodal color distributions (Zepf & Ashman 1993; Ostrov et al. 1993). Since the vast majority of these clusters have been shown to be old (e.g., Strader et al. 2005), the color bimodality implies a corresponding bimodality in metallicity, as is well-established for the Milky Way, where the metal-rich "bulge" and metal-poor "halo" clusters also have distinctly different kinematics and spatial distributions (Harris 2001). This observation is significant because GC formation is widely assumed to accompany the major star forming episodes in a galaxy's history, and therefore the presence of metallicity subpopulations suggests multiple epochs or phases of galaxy assembly that can be explored via their GC tracer populations (e.g., Section 5.4).

From a kinematic point of view, literature studies (e.g., Côté et al. 2003; Richtler et al. 2004; Schuberth et al. 2010; Lee et al. 2010; Woodley et al. 2010a) and more recently SLUGGS data have been used to establish the kinematic distinctiveness of the subpopulations (Strader et al. 2011; Pota et al. 2013), and to identify cases where more than the standard two subpopulations co-exist, due to a more complex or more recent accretion history (Blom et al. 2012a, 2012b; Agnello et al. 2014b). Bimodality is also evident from the different ellipticities of the red and blue GC systems (Park & Lee 2013).

The GC bimodality paradigm has been disputed in favor of a highly nonlinear relation between metallicity and optical color that transforms a unimodal metallicity distribution into a bimodal color distribution (e.g., Yoon et al. 2006, 2011a, 2011b; Blakeslee et al. 2012). This scenario has been tested with near-infrared colors, which should be more linear, and in the few cases with adequate S/N, bimodality was confirmed (Spitler et al. 2008; Chies-Santos et al. 2012a; Cantiello et al. 2014).

The more definitive approach is to measure metallicities via spectroscopy, which has so far not been done with sufficiently large and homogeneous GC data sets for drawing general conclusions (though see Park et al. 2012). We have now addressed this issue in a series of papers using SLUGGS data (Foster et al. 2009, 2011; Alves-Brito et al. 2011; Brodie et al. 2012; Usher et al. 2012). We found that, in old GC populations, our CaT index is insensitive to alpha-element enhancement or horizontal branch morphology and can be reliably used to infer GC metallicities. Using CaT measurements for over 900 GCs in 11 galaxies, we established directly that the GC *metallicity* distributions were typically bimodal—with some cases unclear owing to low-number statistics or to the likely presence of more than two metallicity subpopulations.

Here we note that, as with all aspects of GCs, it is important to exclude the highest-luminosity objects from the analysis since they are heavily contaminated by UCDs—which are likely to be chemically and dynamically distinct (Section 5.3). The natural focus on bright objects in earlier work may account for uncertain conclusions about bimodality (e.g., Cohen et al. 1998). We have also found that the color–metallicity relation is a broken linear function that may vary with host galaxy mass (Usher et al. 2014).

As a summary of these results, Figure 16 (top panel) shows "stacked" GC spectra for eight SLUGGS galaxies. The blue stack contains 390 spectra from GCs with $0.72 < (g - i) < 0.88$ has a S/N = 373 Å^{-1}, and has a CaT-based metallicity of
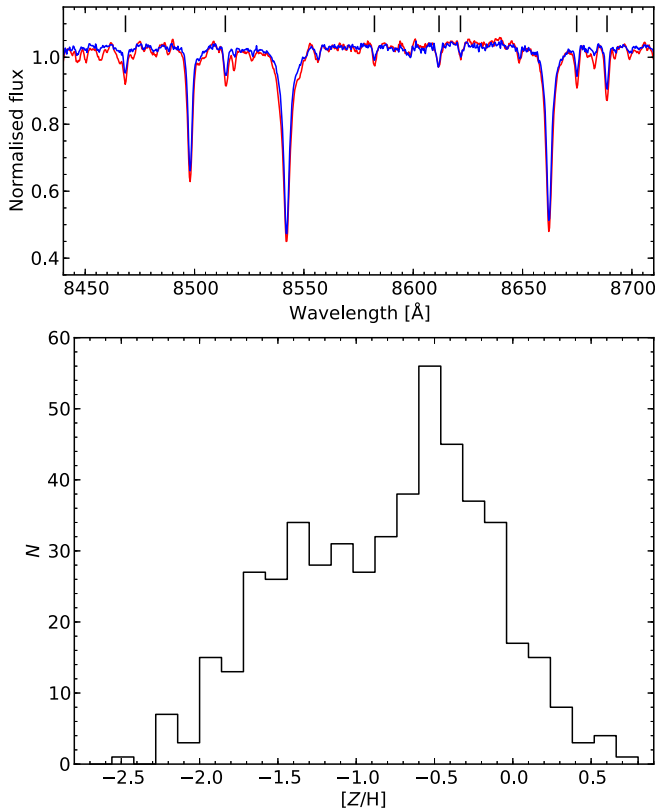

Figure 16. Spectroscopic metallicities of GCs around SLUGGS galaxies. The top panel shows stacks of the spectra around the CaT region for blue and red GC subsamples, with some of the iron lines marked. The difference in metallicity between the two stacked spectra is apparent in the different CaT and iron line strengths. The bottom panel shows the distribution of individual GC metallicities derived from the strength of the CaT, showing 502 GCs with $[\Delta Z/H] < 0.3$ dex. Statistically, bimodality is strongly preferred over unimodality.

(A color version of this figure is available in the online journal.)

$[Z/H] = -1.2$. The red stack contains 353 spectra from GCs with $1.00 < (g - i) < 1.16$, has S/N = 419 Å^{-1}, and has a CaT-based metallicity of $[Z/H] = -0.4$. The two stacks differ not only in their CaT line strengths but also in the strengths of the interspersed, weaker iron lines (marked in the figure), confirming that the CaT is a direct tracer of metallicity. We are now further exploring the dependencies of other weak metal lines (such as Na, Mg, Ti) on metallicity, the IMF, and GC mass (Usher et al. 2014).

The bottom panel of Figure 16 shows the spectroscopic metallicity distribution for all 502 GCs with high quality data ($\Delta[Z/H] < 0.3$ dex) from a total of 11 galaxies from Usher et al. (2012, 2013). The individual galaxies show metallicity bimodality, which persists in the stacked distribution (no shifts were applied before stacking since the metallicity peaks for each galaxy were all at similar locations). Using the Gaussian mixture modeling code of Muratov & Gnedin (2010), the χ^2 fit, peak separation, and kurtosis of the distribution all strongly prefer bimodality to unimodality, with $p < 0.001$, $p = 0.158$, and $p = 0.001$, respectively. The code fitted peaks of $[Z/H] = -1.47 \pm 0.07$ and -0.45 ± 0.05 dex. Very similar results are obtained using the full sample of 908 GCs.

In summary, GC bimodality is supported by spectroscopic metallicities and the spatial distributions and kinematics of GC systems. Although nonlinear relations between color and metallicity might in principle play a minor role in shaping GC

color distributions, and the GC color/metallicity distributions of galaxies may occasionally not distinctly reveal the underlying GC subpopulations (e.g., due to a more complex accretion history), the evidence strongly supports the result that the widely observed color bimodality is a true reflection of distinct subpopulations with inherently different mean metallicities.

5.3. The Nature of Ultra-compact Dwarfs

UCDs, compact spheroidal objects too large to fit within the general classification of GCs, were predicted two decades ago to exist as the remnant nuclei of tidally stripped galaxies (Bassino et al. 1994), and were subsequently confirmed by observations in the Virgo and Fornax clusters (Hilker et al. 1999; Drinkwater et al. 2000). Since that time there have been sustained observational efforts to understand whether these objects actually are stripped nuclei (generally from dwarf ellipticals, but possibly also from compact ellipticals) or are extended star clusters—or both (e.g., Da Rocha et al. 2011; Norris & Kannappan 2011). Accumulating a large catalog of UCDs to begin studying them as a population is contingent on ascertaining their distances—usually through spectroscopy. SLUGGS thus provides a key opportunity to advance the UCD inventory by selecting suitable candidates as targets along with normal GCs in our DEIMOS masks.

Some results to date from SLUGGS and associated work include the first UCD found around a non-cluster galaxy (Hau et al. 2009); the discovery of a new class of UCD, fainter than any UCDs previously studied (Strader et al. 2011; Brodie et al. 2011); the extension of objects into the so-called zone of avoidance in the size–luminosity plane for galaxies, UCDs and star clusters (Forbes et al. 2013); as well as the discoveries of the densest known GC (Foster et al. 2011) and the densest known galaxy (Strader et al. 2013), which heralded a link between the UCD and cE populations (Norris et al. 2014; see Figures 17 and 18).

These results have eroded the classical distinction between star clusters and galaxies, since objects are now found to exist with a continuum of structural properties intermediate to these two populations. Deciphering the evolutionary pathways becomes the next challenge after mapping out parameter space. The UCD population appears to consist of both massive star clusters and stripped galaxies, with a ratio that changes across the size–luminosity diagram (e.g., even objects with classical GC-like sizes of ∼4 pc could originate from stripped nuclei; Pfeffer & Baumgardt 2013).

5.4. New Constraints on Globular Cluster Formation

Given the central place of GCs in our efforts to understand the assembly of galaxies in the SLUGGS survey, it is worthwhile to revisit current thinking on the formation of GCs themselves. We take as our starting place the review of Brodie & Strader (2006), while noting that the earlier reviews of Ashman & Zepf (1998) and Harris (2001) still offer useful insights.

Brodie & Strader (2006) discussed the universal appearance of at least two subpopulations of GCs in all but the least massive galaxies, arguing that the metal-poor GCs likely formed at very high redshift ($z \sim 10$–15; Elmegreen et al. 2012), while the metal-rich GCs originated either in the dissipational merging that formed the main field star population of the host galaxy (at $z \gtrsim 2$ for L^* ETGs; e.g., Kruijssen et al. 2012), or/and in clumpy star formation regions in turbulent galaxies (Kravtsov & Gnedin 2005; Shapiro et al. 2010). This scenario was consistent
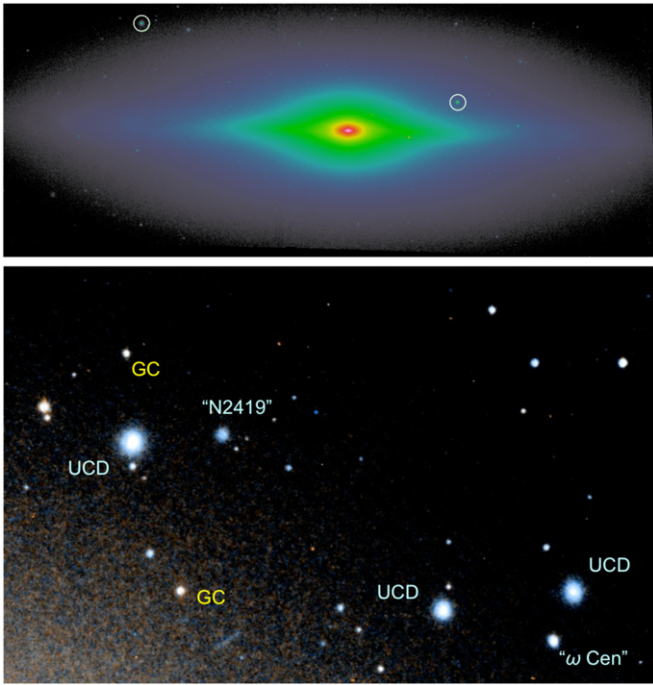
Figure 17. Images of UCDs around SLUGGS galaxies, from *HST*/ACS. Top panel: NGC 3115, a field lenticular galaxy, with two newly spectroscopically confirmed UCDs marked with circles (NGC 3115-UCD1 at upper left, and NGC 3115-AIMSS1 at right; Jennings et al. 2014; Norris et al. 2014). Although such UCDs are bright enough to be seen in century-old photographs (e.g., Pease 1917), their nature was only recognized through recent serendipitous spectroscopy. Bottom panel: a zoomed-in region of the M87 inner halo, showing a variety of compact stellar systems, including GCs, an ω Cen analog, three "classical" UCDs, and a low-luminosity UCD analogous to NGC 2419 (Brodie et al. 2011).

(A color version of this figure is available in the online journal.)

Figure 18. Size–magnitude diagram of distance-confirmed compact stellar systems, showing the *V*-band absolute magnitude, and the projected half-light radius. The data shown are a compilation begun in Brodie et al. (2011), with many more additions from the literature (Usher et al. 2013; Forbes et al. 2013; Norris et al. 2014; Jennings et al. 2014), and includes ∼1070 sub-galactic objects. (Electronic catalog available at http://sages.ucolick.org/spectral_database.html.) Schematic labels are provided for different types of object (globular clusters, ultracompact dwarfs, extended clusters, dwarf spheroidals, compact ellipticals), although we emphasize that the boundaries and distinctions between these separate populations are rather arbitrary. It is a motivation of this work to better understand the properties of the various types of stellar systems and how they relate to one another in a physically motivated classification scheme. Three objects of particular interest are highlighted by black symbols. ω Cen (star symbol) is the nearest example of a GC–UCD transition object. NGC 2419 (square) is the nearest example of a low-luminosity UCD. N4494-UCD1 (triangle) and M60-UCD1 (circle) are the densest known GC and galaxy, respectively.

with the ages, metallicities, numbers, and spatial distributions of the GCs in each subpopulation (where the spatial distributions along with the kinematics are a reflection of the GC orbits). *These are four fundamental observational constraints that must all be reproduced* for any model to be wholly successful in explaining the formation of GC systems (and ultimately of the host galaxies themselves).[14]

Subsequent work has clarified and confirmed aspects of this picture while other parts have held up less well. As discussed in Section 5.2, in-depth spectroscopic work has confirmed GC bimodality, which has become a recognized benchmark for modeling the formation of GC systems. As the general field of galaxy formation has shifted over the years from a focus on major mergers to a two-phase assembly paradigm—with early in situ star formation and later satellite accretion—the context and implications of GC modeling have shifted as well (e.g., Beasley et al. 2002; Prieto & Gnedin 2008; Muratov & Gnedin 2010; Tonini 2013; Katz & Ricotti 2014; Li & Gnedin 2014). Where it had been difficult to reproduce distinct GC metallicity peaks from major mergers, the "new" minor-merger dominated paradigm lends itself more naturally to bimodality, with the metal-rich and metal-poor populations forming predominantly in the host and accreted galaxies, respectively.

However, while the models have now succeeded relatively well in reproducing GC metallicity distributions, they have to

some extent neglected the other critical constraints of ages and orbital distributions, which have also been firmed up over the years. The compilations of spectroscopic age estimates by Puzia et al. (2005) and Strader et al. (2005) have been reinforced by subsequent findings of generally old GCs in ETGs (e.g., Pierce et al. 2006a, 2006b; Cenarro et al. 2007; Norris et al. 2008; Woodley et al. 2010b; Chies-Santos et al. 2012b; Colucci et al. 2013).[15] However, there are also important novelties from studies of the Milky Way, whose GC system is assumed to be broadly analogous to those of ETGs. Here, while isochrone fitting of GCs suggests ages ranging from ∼11 to 13.5 Gyr (formation epochs of $z \sim 2.5$–20; Dotter et al. 2011; Leaman et al. 2013), more precise ages are now claimed based on the white dwarf cooling sequence (Hansen et al. 2007, 2013; Bedin et al. 2009). From studies of one metal-rich and two metal-poor Milky Way GCs, it is inferred that they formed at $z \sim 2$ and 3, respectively. These conclusions fit in nicely with the existing

---

[14] Other basic constraints more closely tied to the internal properties of GCs are the chemical abundance patterns, sizes, luminosity functions, and the correlations of these properties with the GC orbits.
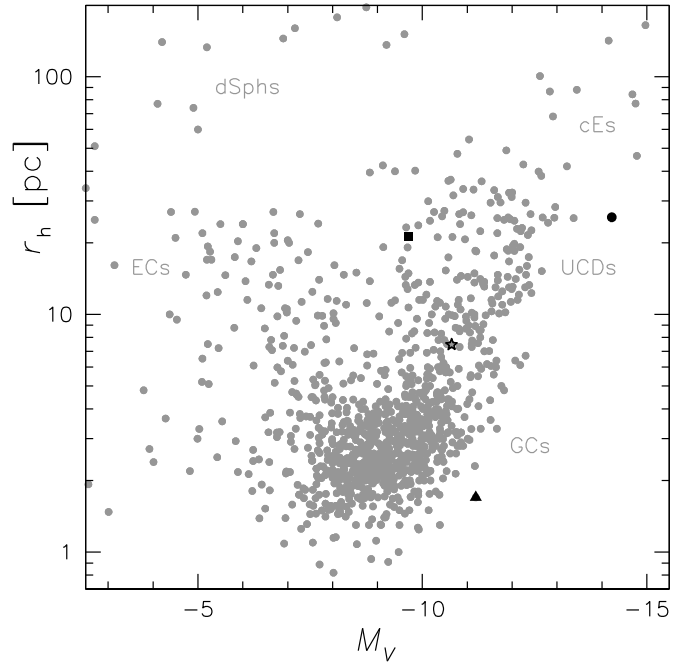
[15] These results are based almost exclusively on low-resolution optical spectra, where there is a long-standing degeneracy in distinguishing young GCs from old ones with blue horizontal branches (e.g., Burstein et al. 1984; de Freitas Pacheco & Barbuy 1995; Cohen et al. 2003). This issue has now become very concrete with the dawning recognition that among massive GCs (the typical targets for age studies), helium-enriched blue horizontal branches are probably very common (e.g., Georgiev et al. 2012; Milone et al. 2014). Hence occasional claims of more pervasive populations of young GCs—without accounting for horizontal branch effects as well as selection biases—should be regarded as inconclusive (Park et al. 2012).

picture for the metal-rich GCs—but not for "cosmological" (very high z) formation for the metal-poor GCs.

The small number statistics here are obviously problematic for drawing general conclusions about the overall Milky Way GC system, much less the GCs of ETGs. Moreover, since galaxies began forming at $z > 7.5$ (Finkelstein et al. 2013), some 13 Gyr ago, it is likely that at least some metal-poor GCs also formed this early. However, if most metal-poor GCs did share a $z \sim 3$ formation epoch, then this would present a severe challenge to any model that forms them mainly in association with low-mass dark matter subhalos or dwarf galaxies that are subsequently assembled into larger galaxies. There is a well-established method for connecting the collapse epochs of subhalos with their spatial and orbital distributions at $z = 0$, with the implication for metal-poor GCs that they must have formed very early, at $z \sim 9$–11, based on their tightly bound orbits (Diemand et al. 2005; Moore et al. 2006; Spitler et al. 2012; Corbett Moran et al. 2014). This issue has been noticed in cosmologically motivated models that form GCs at later epochs, where the spatial distribution was found to be much too extended compared to observations (Prieto & Gnedin 2008; a similar problem is implied for the models of Tonini 2013).

Besides the ages issue, there is also the anisotropy puzzle discussed in Section 5.1, wherein the metal-poor GCs are not observed to follow radially biased orbits as expected in accretion scenarios. The overall implication seems to be that a large fraction of these GCs formed in situ within the host galaxy, in a burst of metal-poor star formation that is missing from current models.

This inference seems to mesh nicely with observational evidence in the Milky Way for inner and outer components of the metal-poor stellar halo (Carollo et al. 2007), which have been explained through cosmological hydrodynamical simulations as in situ and accreted components (Zolotov et al. 2009; Font et al. 2011; Tissera et al. 2014). A dual origin for the metal poor GCs is further supported by observed correlations between ages, metallicities, and orbits (Marín-Franch et al. 2009; Forbes & Bridges 2010; Keller et al. 2012), and between metallicity and galactocentric radius, with steep central gradients that transition to constant mean metallicities in the outer parts—both in the Milky Way and in ETGs (Harris 2001; Forbes et al. 2011).

This metallicity gradient behavior has also been observed for metal-rich GCs (Forbes et al. 2011), and taken together, the evidence from GCs suggests *three* phases of galaxy formation: early in situ metal-poor starbursts, later metal-rich central starbursts, and finally accretion of mixed-metallicity satellites.

The central metal-rich starburst phase may be described more specifically in the context of the current understanding of massive galaxy formation, where the bulk of star formation does not occur in major mergers but in situ, where cold streams from the cosmological web feed violently unstable disks at $z \sim 2$ with high star formation rates (e.g., Parry et al. 2009; Dekel et al. 2009; Hopkins & Hernquist 2010). These disks are thought to host super-giant molecular clouds that are natural sites for GC formation (Shapiro et al. 2010), providing a tidy explanation for the origin of many metal-rich GCs.

The appeal of this "wild-disk" metal-rich GC formation scenario is enhanced by contrasting it with the more traditional merger-formation scenario, as in Muratov & Gnedin (2010). Here most of the metal-rich GCs date from $z < 1$, with very few from $z > 2$, in marked contrast with the data on GC ages (Dotter et al. 2011; but see also Griffen et al. 2010, who were able to reproduce older GCs through mergers). The merger model does

appear successful in at least reproducing the "young" branch of the Milky Way GC age–metallicity relation, but such a relation is probably generic to scenarios of protracted GC formation epochs, e.g., within dwarf galaxies that are later accreted.[16]

These developments from the last half-decade represent emerging insights into the mysterious origins of GCs, and of galaxies in general, while the full picture still remains elusive. We expect that substantial further progress will be made through considering the full chemodynamical constraints from the entire SLUGGS sample.

6. CONCLUSIONS

We have here described the scientific motivation and technical details of the SLUGGS survey, whose unique strength is the collection of data to unprecedentedly wide fields of view around a statistically interesting set of galaxies covering a broad parameter base. The data include 2D maps of galaxy starlight kinematics and metallicities out to three effective radii, complemented and extended by imaging and spectroscopy of GCs out to eight effective radii.

Many papers have already been published in connection with the survey and more are in active preparation. They address a wide variety of scientific questions that ultimately relate to our understanding of the star formation and assembly histories of galaxies. The brief overview of selected results given above reinforces the validity of the original drivers for the work: the inner regions of galaxies are poor predictors of the behavior of the outer regions, which furthermore contain the relics, albeit often well-hidden in the positional–kinematic–metallicity phase-space, of the formation history of the entire galaxy.

Although the sampled number of galaxies is modest, the particular strengths of SLUGGS are its superior velocity resolution and radial extent over any existing 2D chemodynamical survey of ETGs. These advantages will be important for interpreting data from future large surveys (e.g., MaNGA; Section 1.2); the synergy between wide radial extent for representative galaxies and large statistical samples promises robust insights into the assembly histories of galaxies over a wide range of masses and environments.

---

[16] The latest merger-based models from Li & Gnedin (2014) appear to predict older ages for metal-rich GCs around ETGs than the earlier work predicted for the Milky Way. It remains to be seen how these models compare in detail with the GC age–metallicity relations both in the Milky Way and in ETGs (accounting for different galaxy masses and environments, and also comparing to GC ages data that are not specifically selected for youth).

APPENDIX

Here we describe some further details of the galaxy sample parameters, as discussed in Section 2 and adopted in Figure 5 and Table 2.

1. M_K. The K-band absolute magnitudes are derived from the 2MASS extended source catalog (Jarrett et al. 2000), using the extrapolated magnitude parameter k_m_ext. This magnitude is extinction-corrected using the procedure described in Cappellari et al. (2011). An exception is NGC 2974, whose 2MASS photometry is severely impacted by a bright foreground star, and instead we adopt the M_K value from ATLAS^{3D} (Cappellari et al. 2011), who used their own I-band photometry (Cappellari et al. 2006) and an assumed $I-K$ color to correct to K-band (M. Cappellari 2014, private communication; NGC 4486A was the other ATLAS^{3D} galaxy similarly affected and corrected). See Section 2 for further caveats about the 2MASS magnitudes.

2. D. For the distances, we adopt estimates based on SBFs, using the *HST*-based work of Blakeslee et al. (2009) for galaxies in the vicinity of Virgo, and the ground-based work of Tonry et al. (2001) otherwise, after subtracting a distance modulus of -0.06 mag. Note that ATLAS^{3D} used Mei et al. (2007) for the Virgo galaxies, while we have followed the recalibration of Blakeslee et al. (2009). For most galaxies, this makes a difference of less than 0.1 Mpc (1% in distance), but for the brightest galaxies such as M87, the changes are up to $\sim$1 Mpc ($\sim$5% in distance, $\sim$10% in luminosity). We have also estimated a distance to the Virgo A sub-cluster (centered on M87), following Mei et al. (2007) by averaging the distances of all 32 galaxies within $2°$ of M87, and finding 16.7 ± 0.2 Mpc—which is nicely consistent with the 16.7 ± 0.6 Mpc distance to M87 itself, and to other results on the M87 distance (Bird et al. 2010).
NGC 1400 and NGC 1407 in the Eridanus A group are another case of special concern, as a wide range of distances to these galaxies has been used in the literature. The very high relative velocities of the two galaxies suggest that they are very close in line-of-sight distance, so we use the same, averaged distance of 26.8 Mpc for both galaxies, based on Tonry et al. (2001). Note that a further adjustment for data quality (Blakeslee et al. 2010) would imply a distance of 26.5 Mpc, while an *HST*-based distance to NGC 1407 from Cantiello et al. (2005), after recalibration to the distance to NGC 1344 in Blakeslee et al. (2009), gives 26.3 Mpc. However, for the sake of homogeneity with the other galaxies in our sample, we do not apply these minor corrections.

3. σ. For the central stellar velocity dispersion, we use the value within 1 kpc from ATLAS^{3D}, σ_{kpc} (Cappellari et al. 2013). For the non-ATLAS^{3D} galaxies, we use the central velocity dispersion vdis from HyperLeda, applying the calibration reported by ATLAS^{3D}, $\sigma_{kpc} \simeq (\sigma/0.55 \,\mathrm{km\,s^{-1}})^{0.892}$. Note that this calibration deviates systematically for the highest σ galaxies, perhaps owing to template issues with alpha-element enhanced stellar populations, but this issue is not significant for the purposes of sample selection.

4. V/σ. To characterize the rotation, we use $V/\sigma_{e/2}$ from ATLAS^{3D} (Emsellem et al. 2011), which is the aperture-averaged value of rotation divided by dispersion with $0.5\,R_e$. Galaxies with low and high degrees of rotational support have $V/\sigma_{e/2} \sim 0$ and $\sim$1, respectively. We do *not* use the value within $1\,R_e$ as reported by ATLAS^{3D}, since the SAURON kinematics measurements did not actually extend out to $1\,R_e$ for many galaxies, and in particular not for galaxies in the L^* and brighter luminosity range that is the focus of SLUGGS (cf. Figure 1 in Arnold et al. 2014). For the non-ATLAS^{3D} galaxies, we use an approximate calibration for V/σ (Equation (23) of Cappellari et al. 2007) based on long-slit data (e.g., van der Marel et al. 1994).

5. R_e. The effective radii are taken from a calibrated average of 2MASS and RC3 results (de Vaucouleurs et al. 1991), as discussed in Cappellari et al. (2013). Note that these values are adopted for the sake of uniformity and not for accuracy. For the brightest galaxies in particular (NGC 4365, NGC 4374, NGC 4486, NGC 4649), the effective radii derived through deeper optical imaging are twice as large (Kormendy et al. 2009), which should be taken into account for more detailed studies, e.g., dynamical modeling.

6. Morph., T_{Hub}. The galaxy morphologies (E, S0, etc.) are taken from NED, combining the RC3 and RSA classifications (since these sometimes disagree). The Hubble stage parameter T_{Hub} is taken from the morphological type code of HyperLeda (Paturel et al. 2003). The exception is NGC 2974, for which we add a partial S0 classification since it hosts spiral arms and was classified as an S0 or Sa by all six observers (including G. de Vaucouleurs) in Naim et al. (1995). We also assign it the numerical value of $T_{Hub} = -2.1$.

7. P.A., ϵ. The photometric position angles and ellipticities are taken from Krajnović et al. (2011) for the ATLAS^{3D} galaxies, where it represents the large-scale values in the r-band, at typically 2.5–3 R_e. The alternative values of ϵ_e (average within $1\,R_e$) used elsewhere in ATLAS^{3D} do not capture well the overall shapes of the galaxies, e.g., $\epsilon_e = 0.36$ for the near edge-on lenticular galaxy, NGC 1023, as compared to 0.63 from the outer isophotes. For the non-ATLAS^{3D} galaxies, we take the values from the RC3.

8. a_4/a. This parameter represents the fourth-order isophote shape, in percent deviation from a perfect ellipse. Negative values trace boxiness, and positive values trace diskiness. For the ATLAS^{3D} galaxies, the values as used in Emsellem et al. (2011) are taken from the survey Web site.[17] Note that these values are weighted averages within $1\,R_e$ and do not necessarily represent the overall galaxy properties. For the non-ATLAS^{3D} galaxies, approximate values for the central regions are obtained from the Carnegie–Irvine Galaxy Survey (Li et al. 2011).

9. γ'. The central logarithmic density negative slope of the stellar surface brightness profile is taken for the ATLAS^{3D} galaxies from Krajnović et al. (2013). Cored galaxies have $\gamma' < 0.3$, cusped galaxies have $\gamma' > 0.5$, and other galaxies

_____

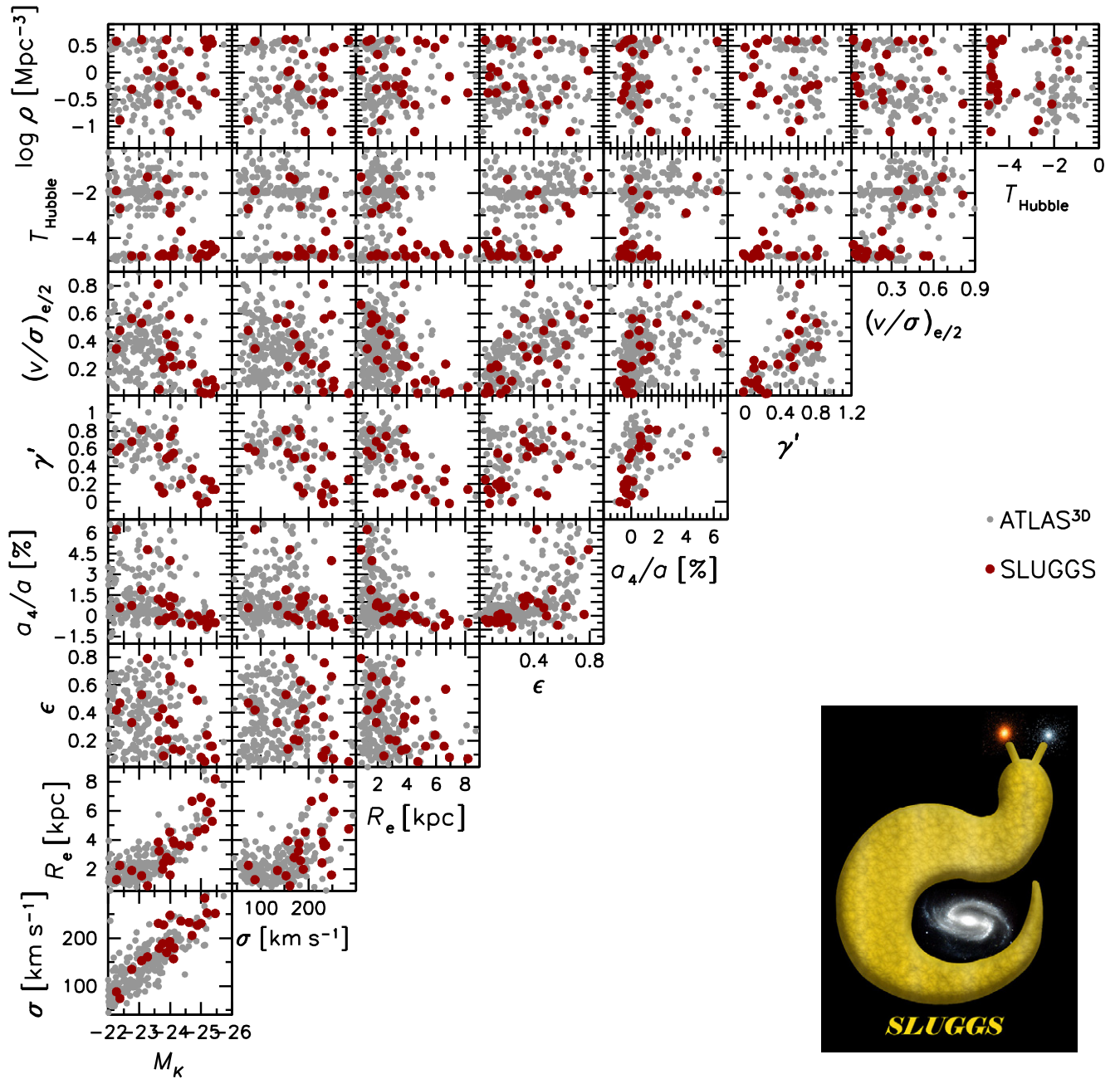[17] http://www-astro.physics.ox.ac.uk/atlas3d/

21

Figure 19. Multi-dimensional parameter space of early-type galaxies in the nearby universe. Red points are from the SLUGGS survey; smaller gray points are from ATLAS[3D]. In broad terms, three main classes of galaxies may be recognized (cf. Kormendy & Bender 1996), with the associated SLUGGS galaxies as follows: boxy, round, massive, centrally slowly rotating ellipticals with central stellar cores: NGCs 720, 1407, 3608, 4365, 4374, 4486, 4649, 5846; disky, flattened, less massive, centrally fast-rotating ellipticals with central stellar cusps: NGCs 821, 1400, 2768, 3377, 4278, 4473, 4494, 4564, 4697; lenticulars: NGCs 1023, 2974, 3115, 4111, 4459, 4474, 4526, 7457. In spite of the limited pool of galaxy candidates in the very nearby universe ($D \lesssim 25$ Mpc), our sample provides excellent coverage of galaxy parameter space (see main text for detailed description).

(A color version of this figure is available in the online journal.)

are intermediate. For the non-ATLAS[3D] galaxies, we draw from Lauer et al. (2007), Spolaor et al. (2008), and Rusli et al. (2013).

10. V_{sys}. The systemic velocity is taken from ATLAS[3D] (Cappellari et al. 2011), and otherwise from NED.

11. ρ_{env}, Env. The environmental density is expressed in number of galaxies per Mpc³ and is taken from the Tully (1988) Nearby Galaxies Catalogue (this parameter is available for the full SLUGGS sample and for 59% of the ATLAS[3D] sample). The densities for NGC 1400 and NGC 1407 arguably ought to be higher, with the high relative velocity

reflecting a recent infall of NGC 1400 rather than a large physical separation (see Romanowsky et al. 2009; Su et al. 2014). To address this issue, we have given NGC 1400 the same ρ_{env} as NGC 1407. The galaxies are also classified as cluster, group, or field members according to their group assignments by Tully, where we assign galaxies to the field if there is no other group member with at least one-third its luminosity. The typical log ρ_{env} values for these categories are 0.5, −0.3, and −1. The "Virgo" galaxy NGC 4365 is assigned to a background group, based on SBF distance measurement.

The full grid of parameter space is shown in Figure 19, with the SLUGGS sample compared to the ATLAS[3D] inventory of galaxies in the nearby universe. Note that the distances (and therefore the magnitudes) of the ATLAS[3D] galaxies in Virgo have been adjusted so as to be consistent with the SLUGGS adopted distances, and the T_{Hub} values of all the ATLAS[3D] galaxies have likewise been updated.

REFERENCES

Abadi, M. G., Navarro, J. F., & Steinmetz, M. 2006, MNRAS, 365, 747
Abazajian, K. N., Adelman-McCarthy, J. K., Agüeros, M. A., et al. 2009, ApJS, 182, 543
Agnello, A., Evans, N. W., & Romanowsky, A. J. 2014a, MNRAS, 442, 3284
Agnello, A., Evans, N. W., Romanowsky, A. J., & Brodie, J. P. 2014b, MNRAS, 442, 3299
Alves-Brito, A., Hau, G. K. T., Forbes, D. A., et al. 2011, MNRAS, 417, 1823
Amorisco, N. C., Agnello, A., & Evans, N. W. 2013, MNRAS, 429, L89
Armandroff, T. E., & Zinn, R. 1988, AJ, 96, 92
Arnold, J. A., Romanowsky, A. J., Brodie, J. P., et al. 2011, ApJL, 736, L26
Arnold, J. A., Romanowsky, A. J., Brodie, J. P., et al. 2014, ApJ, 791, 80
Ashman, K. M., & Zepf, S. E. 1998, Globular Cluster Systems (New York: Cambridge Univ. Press)
Baba, H., Yasuda, N., Ichikawa, S., et al. 2002, in ASP Conf. Ser. 281, Astronomical Data Analysis Software and Systems XI, ed. D. A. Bohlender, D. Durand, & T. H. Handley (San Francisco, CA: ASP), 298
Bassino, L. P., Muzzio, J. C., & Rabolli, M. 1994, ApJ, 431, 634
Baumgardt, H. 1998, A&A, 330, 480
Beasley, M. A., Baugh, C. M., Forbes, D. A., Sharples, R. M., & Frenk, C. S. 2002, MNRAS, 333, 383
Bedin, L. R., Salaris, M., Piotto, G., et al. 2009, ApJ, 697, 965
Bédorf, J., & Portegies Zwart, S. 2013, MNRAS, 431, 767
Behroozi, P. S., Wechsler, R. H., & Conroy, C. 2013, ApJ, 770, 57
Bekki, K., Yahagi, H., Nagashima, M., & Forbes, D. A. 2008, MNRAS, 387, 1131
Bird, S., Harris, W. E., Blakeslee, J. P., & Flynn, C. 2010, A&A, 524, A71
Blakeslee, J. P., Cantiello, M., Mei, S., et al. 2010, ApJ, 724, 657
Blakeslee, J. P., Cho, H., Peng, E. W., et al. 2012, ApJ, 746, 88
Blakeslee, J. P., Jordán, A., Mei, S., et al. 2009, ApJ, 694, 556
Blom, C., Forbes, D. A., Brodie, J. P., et al. 2012a, MNRAS, 426, 1959
Blom, C., Forbes, D. A., Foster, C., Romanowsky, A. J., & Brodie, J. P. 2014, MNRAS, 439, 2420
Blom, C., Spitler, L. R., & Forbes, D. A. 2012b, MNRAS, 420, 37
Boroson, B., Kim, D.-W., & Fabbiano, G. 2011, ApJ, 729, 12
Boulade, O., Charlot, X., Abbon, P., et al. 2003, Proc. SPIE, 4841, 72
Bridges, T., Gebhardt, K., Sharples, R., et al. 2006, MNRAS, 373, 157
Brockamp, M., Küpper, A. H. W., Thies, I., Baumgardt, H., & Kroupa, P. 2014, MNRAS, 441, 150
Brodie, J. P., & Huchra, J. P. 1991, ApJ, 379, 157
Brodie, J. P., Romanowsky, A. J., Strader, J., & Forbes, D. A. 2011, AJ, 142, 199
Brodie, J. P., & Strader, J. 2006, ARA&A, 44, 193
Brodie, J. P., Usher, C., Conroy, C., et al. 2012, ApJL, 759, L33
Bryant, J. J., Owers, M. S., Robotham, A. S. G., et al. 2014, MNRAS, submitted (arXiv:1407.7335)
Bullock, J. S., & Johnston, K. V. 2005, ApJ, 635, 931
Burkert, A., & Tremaine, S. 2010, ApJ, 720, 516
Burstein, D., Faber, S. M., Gaskell, C. M., & Krumm, N. 1984, ApJ, 287, 586
Cantiello, M., Blakeslee, J. P., Raimondo, G., et al. 2005, ApJ, 634, 239
Cantiello, M., Blakeslee, J. P., Raimondo, G., et al. 2014, A&A, 564, L3
Cappellari, M. 2008, MNRAS, 390, 71
Cappellari, M., Bacon, R., Bureau, M., et al. 2006, MNRAS, 366, 1126
Cappellari, M., & Emsellem, E. 2004, PASP, 116, 138
Cappellari, M., Emsellem, E., Bacon, R., et al. 2007, MNRAS, 379, 418
Cappellari, M., Emsellem, E., Krajnović, D., et al. 2011, MNRAS, 413, 813
Cappellari, M., McDermid, R. M., Alatalo, K., et al. 2012, Natur, 484, 485
Cappellari, M., Scott, N., Alatalo, K., et al. 2013, MNRAS, 432, 1709
Carollo, D., Beers, T. C., Lee, Y. S., et al. 2007, Natur, 450, 1020
Cenarro, A. J., Beasley, M. A., Strader, J., Brodie, J. P., & Forbes, D. A. 2007, AJ, 134, 391
Cenarro, A. J., Cardiel, N., Gorgas, J., et al. 2001, MNRAS, 326, 959
Chemin, L., de Blok, W. J. G., & Mamon, G. A. 2011, AJ, 142, 109
Chies-Santos, A. L., Larsen, S. S., Cantiello, M., et al. 2012a, A&A, 539, A54

Chies-Santos, A. L., Larsen, S. S., & Kissler-Patig, M. 2012b, MNRAS, 427, 2349
Coccato, L., Arnaboldi, M., & Gerhard, O. 2013, MNRAS, 436, 1322
Coccato, L., Gerhard, O., & Arnaboldi, M. 2010, MNRAS, 407, L26
Coccato, L., Gerhard, O., Arnaboldi, M., et al. 2009, MNRAS, 394, 1249
Coenda, V., Muriel, H., & Donzelli, C. 2009, ApJ, 700, 1382
Cohen, J. G., Blakeslee, J. P., & Côté, P. 2003, ApJ, 592, 866
Cohen, J. G., Blakeslee, J. P., & Ryzhov, A. 1998, ApJ, 496, 808
Colucci, J. E., Fernanda Durán, M., Bernstein, R. A., & McWilliam, A. 2013, ApJL, 773, L36
Cooper, A. P., Cole, S., Frenk, C. S., et al. 2010, MNRAS, 406, 744
Cooper, M. C., Newman, J. A., Davis, M., Finkbeiner, D. P., & Gerke, B. F. 2012, spec2d: DEEP2 DEIMOS Spectral Pipeline, Astrophysics Source Code Library
Corbett Moran, C., Teyssier, R., & Lake, G. 2014, MNRAS, 442, 2826
Cortesi, A., Arnaboldi, M., Coccato, L., et al. 2013, A&A, 549, A115
Côté, P., Marzke, R. O., & West, M. J. 1998, ApJ, 501, 554
Côté, P., McLaughlin, D. E., Cohen, J. G., & Blakeslee, J. P. 2003, ApJ, 591, 850
Côté, P., McLaughlin, D. E., Hanes, D. A., et al. 2001, ApJ, 559, 828
Courteau, S., Cappellari, M., de Jong, R. S., et al. 2014, RvMP, 86, 47
Cressie., N. 1988, MatG, 20, 405
D'Abrusco, R., Fabbiano, G., & Brassington, N. J. 2014, ApJ, 783, 19
Da Rocha, C., Mieske, S., Georgiev, I. Y., et al. 2011, A&A, 525, A86
Daddi, E., Renzini, A., Pirzkal, N., et al. 2005, ApJ, 626, 680
de Freitas Pacheco, J. A., & Barbuy, B. 1995, A&A, 302, 718
de Lorenzi, F., Gerhard, O., Coccato, L., et al. 2009, MNRAS, 395, 76
de Vaucouleurs, G., de Vaucouleurs, A., Corwin, H. G. Jr., et al. 1991, Third Reference Catalogue of Bright Galaxies (New York: Springer)
de Zeeuw, P. T., Bureau, M., Emsellem, E., et al. 2002, MNRAS, 329, 513
Deason, A. J., Belokurov, V., Evans, N. W., & McCarthy, I. G. 2012, ApJ, 748, 2
Dekel, A., Birnboim, Y., Engel, G., et al. 2009, Natur, 457, 451
Dekel, A., & Burkert, A. 2014, MNRAS, 438, 1870
Dekel, A., Stoehr, F., Mamon, G. A., et al. 2005, Natur, 437, 707
Devereux, N., Willner, S. P., Ashby, M. L. N., Willmer, C. N. A., & Hriljac, P. 2009, ApJ, 702, 955
Diaz, A. I., Terlevich, E., & Terlevich, R. 1989, MNRAS, 239, 325
Diemand, J., Madau, P., & Moore, B. 2005, MNRAS, 364, 367
Dirsch, B., Richtler, T., Geisler, D., et al. 2003, AJ, 125, 1908
Dotter, A., Sarajedini, A., & Anderson, J. 2011, ApJ, 738, 74
Douglas, N. G., Arnaboldi, M., Freeman, K. C., et al. 2002, PASP, 114, 1234
Drinkwater, M. J., Jones, J. B., Gregg, M. D., & Phillipps, S. 2000, PASA, 17, 227
D'Souza, R., Kauffman, G., Wang, J., & Vegetti, S. 2014, MNRAS, 443, 1433
Durrell, P. R., Côté, P., Peng, E. W., et al. 2014, ApJ, 794, 103
Dutton, A. A., & Macciò, A. V. 2014, MNRAS, 441, 3359
Elmegreen, B. G., Malhotra, S., & Rhoads, J. 2012, ApJ, 757, 9
Emsellem, E., Cappellari, M., Krajnović, D., et al. 2011, MNRAS, 414, 888
Faber, S. M., Phillips, A. C., Kibrick, R. I., et al. 2003, Proc. SPIE, 4841, 1657
Fakhouri, O., Ma, C.-P., & Boylan-Kolchin, M. 2010, MNRAS, 406, 2267
Fall, S. M., & Efstathiou, G. 1980, MNRAS, 193, 189
Fall, S. M., & Romanowsky, A. J. 2013, ApJL, 769, L26
Fall, S. M., & Zhang, Q. 2001, ApJ, 561, 751
Ferrarese, L., Côté, P., Cuillandre, J.-C., et al. 2012, ApJS, 200, 4
Finkelstein, S. L., Papovich, C., Dickinson, M., et al. 2013, Natur, 502, 524
Font, A. S., McCarthy, I. G., Crain, R. A., et al. 2011, MNRAS, 416, 2802
Forbes, D. A., & Bridges, T. 2010, MNRAS, 404, 1203
Forbes, D. A., Cortesi, A., Pota, V., et al. 2012, MNRAS, 426, 975
Forbes, D. A., Pota, V., Usher, C., et al. 2013, MNRAS, 435, L6
Forbes, D. A., Sánchez-Blázquez, P., Phan, A. T. T., et al. 2006, MNRAS, 366, 1230
Forbes, D. A., Spitler, L. R., Strader, J., et al. 2011, MNRAS, 413, 2943
Forbes, D. A., & Thomson, R. C. 1992, MNRAS, 254, 723
Forte, J. C., Faifer, F., & Geisler, D. 2007, MNRAS, 382, 1947
Forte, J. C., Martinez, R. E., & Muzzio, J. C. 1982, AJ, 87, 1465
Forte, J. C., Vega, E. I., Faifer, F. R., et al. 2014, MNRAS, 441, 1391
Foster, C., Arnold, J. A., Forbes, D. A., et al. 2013, MNRAS, 435, 3587
Foster, C., Forbes, D. A., Proctor, R. N., et al. 2010, AJ, 139, 1566
Foster, C., Lux, H., Romanosky, A. J., et al. 2014, MNRAS, 442, 3544
Foster, C., Pastorello, N., Roediger, J., et al. 2015, MNRAS, submitted
Foster, C., Proctor, R. N., Forbes, D. A., et al. 2009, MNRAS, 400, 2135
Foster, C., Spitler, L. R., Romanowsky, A. J., et al. 2011, MNRAS, 415, 3393
Frenk, C. S., & White, S. D. M. 1980, MNRAS, 193, 295
Gabor, J. M., & Davé, R. 2012, MNRAS, 427, 1816
Gebhardt, K., & Thomas, J. 2009, ApJ, 700, 1690

Georgiev, I. Y., Goudfrooij, P., & Puzia, T. H. 2012, MNRAS, 420, 1317
Governato, F., Mayer, L., Wadsley, J., et al. 2004, ApJ, 607, 688
Greene, J. E., Murphy, J. D., Graves, G. J., et al. 2013, ApJ, 776, 64
Griffen, B. F., Drinkwater, M. J., Thomas, P. A., Helly, J. C., & Pimbblet, K. A. 2010, MNRAS, 405, 375
Hansen, B. M. S., Anderson, J., Brewer, J., et al. 2007, ApJ, 671, 380
Hansen, B. M. S., Kalirai, J. S., Anderson, J., et al. 2013, Natur, 500, 51
Hargis, J. R., & Rhode, K. L. 2012, AJ, 144, 164
Harris, G. L. H., & Harris, W. E. 2011, MNRAS, 410, 2347
Harris, G. L. H., Poole, G. B., & Harris, W. E. 2014, MNRAS, 438, 2117
Harris, W. E. 2001, in Saas-Fee Advanced Course 28: Star Clusters, ed. L. Labhardt & B. Binggeli (Berlin: Springer), 223
Harris, W. E., Harris, G. L. H., & Alessi, M. 2013, ApJ, 772, 82
Harris, W. E., Harris, G. L. H., Layden, A. C., & Wehner, E. M. H. 2007, ApJ, 666, 903
Harris, W. E., & Racine, R. 1979, ARA&A, 17, 241
Hau, G. K. T., Spitler, L. R., Forbes, D. A., et al. 2009, MNRAS, 394, L97
Hilker, M., Infante, L., Vieira, G., Kissler-Patig, M., & Richtler, T. 1999, A&AS, 134, 75
Hilz, M., Naab, T., Ostriker, J. P., et al. 2012, MNRAS, 425, 3119
Hilz, M., Naab, T., & Ostriker, J. P. 2013, MNRAS, 429, 2924
Hirschmann, M., Naab, T., Ostriker, J. P., et al. 2015, MNRAS, submitted (arXiv:1410.2244)
Hopkins, P. F., Bundy, K., Hernquist, L., Wuyts, S., & Cox, T. J. 2010, MNRAS, 401, 1099
Hopkins, P. F., & Hernquist, L. 2010, MNRAS, 402, 985
Huang, S., Ho, L. C., Peng, C. Y., Li, Z.-Y., & Barth, A. J. 2013, ApJL, 768, L28
Humphrey, P. J., Buote, D. A., Brighenti, F., Gebhardt, K., & Mathews, W. G. 2013, MNRAS, 430, 1516
Hwang, H. S., Lee, M. G., Park, H. S., et al. 2008, ApJ, 674, 869
Ibata, R. A., Lewis, G. F., McConnachie, A. W., et al. 2014, ApJ, 780, 128
Janowiecki, S., Mihos, J. C., Harding, P., et al. 2010, ApJ, 715, 972
Jarrett, T. H., Chester, T., Cutri, R., et al. 2000, AJ, 119, 2498
Jennings, Z. G., Strader, J., Romanowsky, A. J., et al. 2014, AJ, 148, 32
Johansson, P. H., Naab, T., & Ostriker, J. P. 2012, ApJ, 754, 115
Jordán, A., McLaughlin, D. E., Côté, P., et al. 2007, ApJS, 171, 101
Kalirai, J. S., Gilbert, K. M., Guhathakurta, P., et al. 2006, ApJ, 648, 389
Kartha, S. S., Forbes, D. A., Spitler, L. R., et al. 2014, MNRAS, 437, 273
Katz, H., & Ricotti, M. 2014, MNRAS, 444, 2377
Keller, S. C., Mackey, D., & Da Costa, G. S. 2012, ApJ, 744, 57
Khochfar, S., & Silk, J. 2006, ApJL, 648, L21
Kim, D.-W., & Fabbiano, G. 2013, ApJ, 776, 116
Kissler-Patig, M., Forbes, D. A., & Minniti, D. 1998, MNRAS, 298, 1123
Kissler-Patig, M., & Gebhardt, K. 1998, AJ, 116, 2237
Kormendy, J., & Bender, R. 1996, ApJL, 464, L119
Kormendy, J., Fisher, D. B., Cornell, M. E., & Bender, R. 2009, ApJS, 182, 216
Krajnović, D., Bacon, R., Cappellari, M., et al. 2008, MNRAS, 390, 93
Krajnović, D., Cappellari, M., de Zeeuw, P. T., & Copin, Y. 2006, MNRAS, 366, 787
Krajnović, D., Emsellem, E., Cappellari, M., et al. 2011, MNRAS, 414, 2923
Krajnović, D., Karick, A. M., Davies, R. L., et al. 2013, MNRAS, 433, 2812
Kravtsov, A. V., & Gnedin, O. Y. 2005, ApJ, 623, 650
Krige, D. G. 1951, J. Chem., Metal. and Mining Soc. South Africa, 52, 119
Kruijssen, J. M. D., Pelupessy, F. I., Lamers, H. J. G. L. M., et al. 2012, MNRAS, 421, 1927
Kundu, A., & Whitmore, B. C. 2001, AJ, 121, 2950
Kuntschner, H., Emsellem, E., Bacon, R., et al. 2010, MNRAS, 408, 97
La Barbera, F., Ferreras, I., de Carvalho, R. R., et al. 2012, MNRAS, 426, 2300
Lackner, C. N., Cen, R., Ostriker, J. P., & Joung, M. R. 2012, MNRAS, 425, 641
Larsen, S. S., Brodie, J. P., Huchra, J. P., Forbes, D. A., & Grillmair, C. J. 2001, AJ, 121, 2974
Lauer, T. R., Gebhardt, K., Faber, S. M., et al. 2007, ApJ, 664, 226
Leaman, R., VandenBerg, D. A., & Mendel, J. T. 2013, MNRAS, 436, 122
Lee, M. G., Park, H. S., Hwang, H. S., et al. 2010, ApJ, 709, 1083
Li, H., & Gnedin, O. Y. 2014, ApJ, 796, 10
Li, Z.-Y., Ho, L. C., Barth, A. J., & Peng, C. Y. 2011, ApJS, 197, 22
Ma, C.-P., Greene, J. E., McConnell, N., et al. 2014, ApJ, 795, 158
Mamon, G. A., Biviano, A., & Boué, G. 2013, MNRAS, 429, 3079
Mamon, G. A., & Łokas, E. L. 2005, MNRAS, 363, 705
Marín-Franch, A., Aparicio, A., Piotto, G., et al. 2009, ApJ, 694, 1498
Matheron, G. 1963, Economic Geology and the Bulletin of the Society of Economic Geologists, 58, 1246
McMillan, P. J., Athanassoula, E., & Dehnen, W. 2007, MNRAS, 376, 1261
McNeil, E. K., Arnaboldi, M., Freeman, K. C., et al. 2010, A&A, 518, A44
Mei, S., Blakeslee, J. P., Côté, P., et al. 2007, ApJ, 655, 144

Méndez, R. H., Thomas, D., Saglia, R. P., et al. 2005, ApJ, 627, 767
Mestel, L. 1963, MNRAS, 126, 553
Mieske, S., Jordán, A., Côté, P., et al. 2010, ApJ, 710, 1672
Mihos, J. C., Harding, P., Feldmeier, J., & Morrison, H. 2005, ApJL, 631, L41
Mihos, J. C., Harding, P., Rudick, C. S., & Feldmeier, J. J. 2013, ApJL, 764, L20
Milone, A. P., Marino, A. F., Dotter, A., et al. 2014, ApJ, 785, 21
Miyazaki, S., Komiyama, Y., Sekiguchi, M., et al. 2002, PASJ, 54, 833
Monet, D. G., Levine, S. E., Canzian, B., et al. 2003, AJ, 125, 984
Moore, B., Diemand, J., Madau, P., Zemp, M., & Stadel, J. 2006, MNRAS, 368, 563
Mouhcine, M., Ibata, R., & Rejkuba, M. 2011, MNRAS, 415, 993
Muñoz, R. P., Puzia, T. H., Lançon, A., et al. 2014, ApJS, 210, 4
Muratov, A. L., & Gnedin, O. Y. 2010, ApJ, 718, 1266
Murphy, J. D., Gebhardt, K., & Cradit, M. 2014, ApJ, 785, 143
Naab, T., Johansson, P. H., & Ostriker, J. P. 2009, ApJL, 699, L178
Naim, A., Lahav, O., Buta, R. J., et al. 1995, MNRAS, 274, 1107
Napolitano, N. R., Pota, V., Romanowsky, A. J., et al. 2014, MNRAS, 439, 659
Napolitano, N. R., Romanowsky, A. J., Capaccioli, M., et al. 2011, MNRAS, 411, 2035
Navarro, J. F., Frenk, C. S., & White, S. D. M. 1997, ApJ, 490, 493
Navarro, J. F., & Steinmetz, M. 1997, ApJ, 478, 13
Newman, A. B., Treu, T., Ellis, R. S., & Sand, D. J. 2013a, ApJ, 765, 25
Newman, J. A., Cooper, M. C., Davis, M., et al. 2013b, ApJS, 208, 5
Nipoti, C., Treu, T., Leauthaud, A., et al. 2012, MNRAS, 422, 1714
Norris, M. A., & Kannappan, S. J. 2011, MNRAS, 414, 739
Norris, M. A., Kannappan, S. J., Forbes, D. A., et al. 2014, MNRAS, 443, 1151
Norris, M. A., Sharples, R. M., Bridges, T., et al. 2008, MNRAS, 385, 40
Obreschkow, D., & Glazebrook, K. 2014, ApJ, 784, 26
Oh, S.-H., de Blok, W. J. G., Brinks, E., Walter, F., & Kennicutt, R. C., Jr. 2011, AJ, 141, 193
Oñorbe, J., Domínguez-Tenreiro, R., Sáiz, A., & Serna, A. 2007, MNRAS, 376, 39
Oogi, T., & Habe, A. 2013, MNRAS, 428, 641
Oser, L., Ostriker, J. P., Naab, T., Johansson, P. H., & Burkert, A. 2010, ApJ, 725, 2312
Oser, L., Naab, T., Ostriker, J. P., & Johansson, P. H. 2012, ApJ, 744, 63
Ostrov, P., Geisler, D., & Forte, J. C. 1993, AJ, 105, 1762
O'Sullivan, E., Forbes, D. A., & Ponman, T. J. 2001, MNRAS, 328, 461
Ouchi, M., Shimasaku, K., Okamura, S., et al. 2004, ApJ, 611, 660
Park, H. S., & Lee, M. G. 2013, ApJL, 773, L27
Park, H. S., Lee, M. G., Hwang, H. S., et al. 2012, ApJ, 759, 116
Parry, O. H., Eke, V. R., & Frenk, C. S. 2009, MNRAS, 396, 1972
Pastorello, N., Forbes, D. A., Foster, C., et al. 2014, MNRAS, 442, 1003
Paturel, G., Petit, C., Prugniel, P., et al. 2003, A&A, 412, 45
Paudel, S., Duc, P.-A., Côté, P., et al. 2013, ApJ, 767, 133
Pease, F. G. 1917, ApJ, 46, 24
Peng, E. W., Ford, H. C., & Freeman, K. C. 2004a, ApJS, 150, 367
Peng, E. W., Ford, H. C., & Freeman, K. C. 2004b, ApJ, 602, 685
Peng, E. W., Jordán, A., Côté, P., et al. 2006, ApJ, 639, 95
Peng, E. W., Jordán, A., Côté, P., et al. 2008, ApJ, 681, 197
Pfeffer, J., & Baumgardt, H. 2013, MNRAS, 433, 1997
Pierce, M., Beasley, M. A., Forbes, D. A., et al. 2006a, MNRAS, 366, 1253
Pierce, M., Bridges, T., Forbes, D. A., et al. 2006b, MNRAS, 368, 325
Porter, L. A., Somerville, R. S., Primack, J. R., & Johansson, P. H. 2014, MNRAS, 444, 942
Pota, V., Forbes, D. A., Romanowsky, A. J., et al. 2013, MNRAS, 428, 389
Prieto, J. L., & Gnedin, O. Y. 2008, ApJ, 689, 919
Proctor, R. N., Forbes, D. A., Brodie, J. P., & Strader, J. 2008, MNRAS, 385, 1709
Proctor, R. N., Forbes, D. A., Romanowsky, A. J., et al. 2009, MNRAS, 398, 91
Puzia, T. H., Kissler-Patig, M., Thomas, D., et al. 2005, A&A, 439, 997
Raskutti, S., Greene, J. E., & Murphy, J. D. 2014, ApJ, 786, 23
Rhode, K. L. 2012, AJ, 144, 154
Rhode, K. L., & Zepf, S. E. 2001, AJ, 121, 210
Rhode, K. L., Zepf, S. E., Kundu, A., & Larner, A. N. 2007, AJ, 134, 1403
Richtler, T., Dirsch, B., Gebhardt, K., et al. 2004, AJ, 127, 2094
Richtler, T., Hilker, M., Kumar, B., et al. 2014, A&A, 569, A41
Romanowsky, A. J., Douglas, N. G., Arnaboldi, M., et al. 2003, Sci, 301, 1696
Romanowsky, A. J., & Fall, S. M. 2012, ApJS, 203, 17
Romanowsky, A. J., & Kochanek, C. S. 2001, ApJ, 553, 722
Romanowsky, A. J., Strader, J., Brodie, J. P., et al. 2012, ApJ, 748, 29
Romanowsky, A. J., Strader, J., Spitler, L. R., et al. 2009, AJ, 137, 4956
Rusli, S. P., Erwin, P., Saglia, R. P., et al. 2013, AJ, 146, 160
Sales, L. V., Navarro, J. F., Abadi, M. G., & Steinmetz, M. 2007, MNRAS, 379, 1464
Sánchez, S. F., Kennicutt, R. C., Gil de Paz, A., et al. 2012, A&A, 538, A8

Schauer, A. T. P., Remus, R.-S., Burkert, A., & Johansson, P. H. 2014, ApJL, 783, L32

Schlegel, D. J., Finkbeiner, D. P., & Davis, M. 1998, ApJ, 500, 525

Schuberth, Y., Richtler, T., Hilker, M., et al. 2010, A&A, 513, A52

Schuberth, Y., Richtler, T., Hilker, M., et al. 2012, A&A, 544, A115

Scott, N., Graham, A. W., & Schombert, J. 2013, ApJ, 768, 76

Searle, L., & Zinn, R. 1978, ApJ, 225, 357

Sérsic, J. L. 1968, Atlas de galaxias australes (Cordoba, Argentina: Observatorio Astronomico)

Shapiro, K. L., Genzel, R., & Förster Schreiber, N. M. 2010, MNRAS, 403, L36

Sinnott, B., Hou, A., Anderson, R., Harris, W. E., & Woodley, K. A. 2010, AJ, 140, 2101

Skrutskie, M. F., Cutri, R. M., Stiening, R., et al. 2006, AJ, 131, 1163

Snyder, G. F., Hopkins, P. F., & Hernquist, L. 2011, ApJL, 728, L24

Spitler, L. R., & Forbes, D. A. 2009, MNRAS, 392, L1

Spitler, L. R., Forbes, D. A., & Beasley, M. A. 2008, MNRAS, 389, 1150

Spitler, L. R., Larsen, S. S., Strader, J., et al. 2006, AJ, 132, 1593

Spitler, L. R., Romanowsky, A. J., Diemand, J., et al. 2012, MNRAS, 423, 2177

Spolaor, M., Forbes, D. A., Hau, G. K. T., Proctor, R. N., & Brough, S. 2008, MNRAS, 385, 667

Stetson, P. B. 1992, in ASP Conf. Ser. 25, Astronomical Data Analysis Software and Systems I, ed. D. M. Worrall, C. Biemesderfer, & J. Barnes (San Francisco, CA: ASP), 297

Strader, J., Brodie, J. P., Cenarro, A. J., Beasley, M. A., & Forbes, D. A. 2005, AJ, 130, 1315

Strader, J., Brodie, J. P., Spitler, L., & Beasley, M. A. 2006, AJ, 132, 2333

Strader, J., Romanowsky, A. J., Brodie, J. P., et al. 2011, ApJS, 197, 33

Strader, J., Seth, A. C., Forbes, D. A., et al. 2013, ApJL, 775, L6

Su, Y., Gu, L., White, R. E., III, & Irwin, J. 2014, ApJ, 786, 152

Tal, T., van Dokkum, P. G., Nelan, J., & Bezanson, R. 2009, AJ, 138, 1417

Teodorescu, A. M., Méndez, R. H., Bernardi, F., et al. 2011, ApJ, 736, 65

Thomas, J., Saglia, R. P., Bender, R., et al. 2009, ApJ, 691, 770

Tissera, P. B., Beers, T. C., Carollo, D., & Scannapieco, C. 2014, MNRAS, 439, 3128

Tonini, C. 2013, ApJ, 762, 39

Tonry, J. L., Dressler, A., Blakeslee, J. P., et al. 2001, ApJ, 546, 681

Tortora, C., Napolitano, N. R., Romanowsky, A. J., & Jetzer, P. 2010, ApJL, 721, L1

Treu, T., Auger, M. W., Koopmans, L. V. E., et al. 2010, ApJ, 709, 1195

Trujillo-Gomez, S., Klypin, A., Primack, J., & Romanowsky, A. J. 2011, ApJ, 742, 16

Tully, R. B. 1988, Nearby Galaxies Catalog (Cambridge: Cambridge Univ. Press)

Usher, C., Forbes, D. A., Brodie, J. P., et al. 2012, MNRAS, 426, 1475

Usher, C., Forbes, D. A., Brodie, J. P., et al. 2014, MNRAS, in press (arXiv:1409.8676)

Usher, C., Forbes, D. A., Spitler, L. R., et al. 2013, MNRAS, 436, 1172

van der Marel, R. P., Rix, H. W., Carter, D., et al. 1994, MNRAS, 268, 521

van Dokkum, P. G., Kriek, M., & Franx, M. 2009, Natur, 460, 717

Vazdekis, A., Cenarro, A. J., Gorgas, J., Cardiel, N., & Peletier, R. F. 2003, MNRAS, 340, 1317

Ventimiglia, G., Arnaboldi, M., & Gerhard, O. 2011, A&A, 528, A24

Vesperini, E., Zepf, S. E., Kundu, A., & Ashman, K. M. 2003, ApJ, 593, 760

Vitvitska, M., Klypin, A. A., Kravtsov, A. V., et al. 2002, ApJ, 581, 799

Walker, M. G., & Peñarrubia, J. 2011, ApJ, 742, 20

White, S. D. M. 1980, MNRAS, 191, 1P

Woodley, K. A., Gómez, M., Harris, W. E., Geisler, D., & Harris, G. L. H. 2010a, AJ, 139, 1871

Woodley, K. A., & Harris, W. E. 2011, AJ, 141, 27

Woodley, K. A., Harris, W. E., Puzia, T. H., et al. 2010b, ApJ, 708, 1335

Wu, X., Gerhard, O., Naab, T., et al. 2014, MNRAS, 438, 2701

Wu, X., & Kroupa, P. 2013, MNRAS, 435, 1536

Yagi, M., Kashikawa, N., Sekiguchi, M., et al. 2002, AJ, 123, 66

Yang, X., Mo, H. J., van den Bosch, F. C., & Jing, Y. P. 2005, MNRAS, 357, 608

Yoon, S., Yi, S. K., & Lee, Y. 2006, Sci, 311, 1129

Yoon, S.-J., Lee, S.-Y., Blakeslee, J. P., et al. 2011a, ApJ, 743, 150

Yoon, S.-J., Sohn, S. T., Lee, S.-Y., et al. 2011b, ApJ, 743, 149

Zepf, S. E., & Ashman, K. M. 1993, MNRAS, 264, 611

Zolotov, A., Willman, B., Brooks, A. M., et al. 2009, ApJ, 702, 1058